



**TECHNISCHE
UNIVERSITÄT
WIEN**
Vienna University of Technology

Masterarbeit

Holographic entanglement entropy in heavy ion collisions

Ausgeführt am
Institut für Theoretische Physik
der Technischen Universität Wien

unter der Anleitung von
Proj.Ass. Dipl.-Ing. Christian Ecker
und
Assistant Prof. Dr.techn. Daniel Grumiller

durch
Philipp Stanzer
Matrikelnr.:0926979
Mollgasse 13/2
1180 Wien

Wien, am 18.03.2016

Abstract

Using the methods of holography we calculate the two-point function and entanglement entropy in heavy ion collisions, modeled by colliding gravitational shock waves in Anti-de Sitter spacetime. The calculation reduces to finding extremal surfaces (or geodesics, using the symmetry of the investigated boundary region) in the gravitational problem. A Mathematica package, capable of finding geodesics for several different scenarios using relaxation methods, was developed as part of this work. Using two different initial conditions, wide and narrow shock waves, we find qualitatively different behavior of the calculated quantities. This allows to use the entanglement entropy as order parameter to distinguish between the transparency and full stopping scenario of colliding shock waves.

Kurzfassung

Unter Verwendung holographischer Methoden rechnen wir die Zweipunkt-Korrelationsfunktion und die Entanglement Entropie für Schwerionen-Kollisionen aus, welche als Kollision von Gravitationsschockwellen in 5 dimensionaler Anti-de Sitter Raumzeit modelliert werden. Die Berechnung dieser Größen reduziert sich auf der Seite der Gravitationstheorie auf die Berechnung extremaler Flächen (bzw. Geodäten, unter Verwendung der Symmetrie der untersuchten Region). Im Rahmen dieser Arbeit wurde ein Mathematica Package entwickelt, das diese Berechnungen mittels Relaxationsmethoden für verschiedene Szenarios ausführen kann. Unter Verwendung zweier verschiedener Anfangsbedingungen, breiten und schmalen Schockwellen, zeigt sich qualitativ unterschiedliches Verhalten der berechneten Größen. Das erlaubt es, die Entanglement Entropie als Ordnungsparameter für die Unterscheidung zwischen Transparenz und vollem Abstoppen der kollidierenden Schockwellen zu verwenden.

Contents

| | | |
|----------|--|-----------|
| 1 | Introduction | 4 |
| 2 | Preliminaries | 6 |
| 2.1 | Heavy ion collisions | 6 |
| 2.2 | AdS/CFT correspondence | 7 |
| 2.3 | Holographic description of heavy ion collisions | 9 |
| 2.4 | Entanglement entropy | 10 |
| 2.5 | Einstein's equations | 13 |
| 3 | Solving Einstein's equations numerically | 15 |
| 3.1 | Approaches | 15 |
| 3.2 | Homogenous isotropization | 16 |
| 3.2.1 | Asymptotic behavior | 17 |
| 3.2.2 | Redefinition of the metric functions | 18 |
| 3.2.3 | Holographic relations | 19 |
| 3.2.4 | Numerical results | 19 |
| 3.3 | Shock wave setup | 21 |
| 4 | Holographic calculation of two-point functions and entanglement entropy | 28 |
| 4.1 | The two-point function | 29 |
| 4.1.1 | Geodesic ansatz in pure AdS | 29 |
| 4.2 | The holographic entanglement entropy | 31 |
| 4.2.1 | Auxiliary spacetime | 32 |
| 4.2.2 | Geodesic ansatz in the auxiliary spacetime | 33 |

| | | |
|----------|---|-----------|
| 4.3 | Numerical solution of the geodesic equation | 35 |
| 4.3.1 | The relaxation method | 35 |
| 4.3.2 | Implementation for the geodesic equation | 39 |
| 5 | Results | 41 |
| 5.1 | Time evolution of two-point function and entanglement entropy . . | 41 |
| 5.2 | Tracking a shock wave | 46 |
| 5.3 | Correlation of two colliding shocks | 48 |
| 6 | Conclusion and outlook | 50 |
| 6.1 | Conclusion | 50 |
| 6.2 | Outlook | 51 |
| A | The relaxationPackage | 53 |

1 Introduction

In the history of physics, it often turned out to be useful to apply methods developed in one field to some other one, even if there seemed to be no connection in the first place. This can result in the unification of two theories (electricity and magnetism) or reveal dualities (wave-particle), which help to describe phenomena more precisely. Of course, the unification of all interactions is still an open problem many physicists are working on.

These two very different examples encourage to combine three of the most interesting fields of physics in this work. General relativity with black holes and all the other aspects of astrophysics is especially after the detection of gravitational waves a very interesting topic. Already mentioned above, the second field is the unification of interactions, as every physicist has the wish to describe nature with one unified theory for which string theory might be a candidate. The third field involved in this work is high energy physics. With large projects at institutions like CERN amongst others, it is possible to search for supersymmetry and test theories from the experimental point of view.

Similar to a plasma generated by heating up a gas above a certain temperature (energy), there exists a plasma state in nuclear physics. Like nuclei and electrons, which decouple to form the plasma, quarks and gluons are no longer confined to hadrons above a characteristic energy scale and form a so called quark-gluon plasma. To reach this scale of energy density, collision experiments with heavy ions are necessary. At the LHC lead ions are accelerated close to the speed of light and then brought to collision, whereas gold ions are used at RHIC. Providing a large amount of matter compared to single protons, enough energy is created to generate a quark-gluon plasma. Although quantum chromodynamics describes all aspects of this new matter state, it is not possible to perform all calculations within this framework at present. Searching a new framework to allow more calculations, methods of string theory and general relativity are combined to tackle these problems.

This idea has led to the holographic principle and particularly to the AdS/CFT correspondence, which has been used in numerous recent works. Mainly the energy, pressure components and thermalization time of the quark-gluon plasma have been studied. Going beyond that we are interested in the correlations within the system. Therefore we look at quantities like two-point functions and the entanglement entropy (see section 2.4).

Besides all the theoretical aspects of the different fields needed to combine them, also numerical methods are required in this work. Differential equations like Ein-

stein's equations or the geodesic equations of motion need to be solved numerically, since there is no analytic solution known for our system.

This work is organized as follows. In chapter 2 the ingredients of this work are introduced. Principles and methods of high energy physics (i.e. heavy ion collisions), holography (i.e. AdS/CFT correspondence), quantum physics (i.e. entanglement entropy) and general relativity (i.e. Einstein's equations in Anti-de Sitter space), which are used in the remainder of the work are explained. In chapter 3 the methods used to solve Einstein's equations are explained using a simple model, as well as the results for colliding shock waves are presented. The calculation of two-point functions and the entanglement entropy is presented in chapter 4. The results of this calculation are discussed in chapter 5. In chapter 6 a conclusion and thoughts on further interesting calculations and open questions are given. Lastly, the Mathematica package created within this work is described in appendix A.

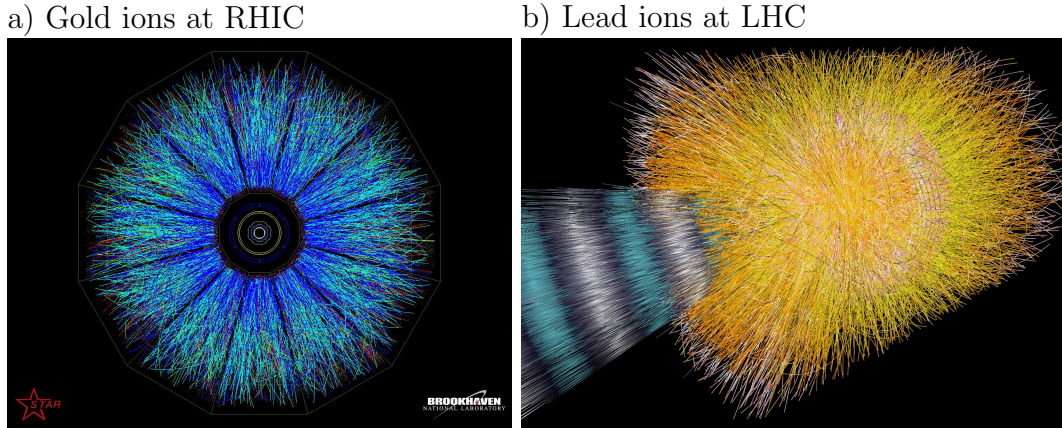


Figure 1: These images display the tracks of particles created in HICs, seen by the detectors STAR (at RHIC [1]) and ALICE (at LHC [2]).

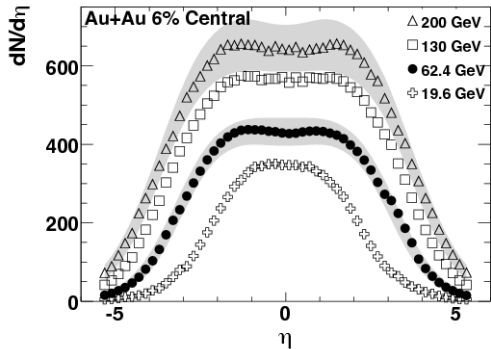
2 Preliminaries

2.1 Heavy ion collisions

In high energy physics collision experiments are carried out at particle accelerators. Instead of elementary particles, for which the processes are understood quite good, at RHIC and partly at LHC heavy ions are used. Such collisions create a greater volume with matter at high energy density to simulate “macroscopic” amounts of matter. The observations show qualitatively new phenomena, different to those resulting from interactions of a few elementary particles. This setup is the only experimental approach to many body quantum chromodynamics (QCD). Gold ions at RHIC and lead ions at LHC are accelerated close to the speed of light and collide with total center of mass energies of about 40 TeV and 600 TeV respectively. The result of such heavy ion collisions (HIC) is the production of a huge amount of particles (see Fig. 2.1 for a schematic illustration). The multiplicities of charged particles produced is shown in Fig. 2. In total this results in about 5000 particles produced at RHIC while this number is five times larger for the energies reached at LHC.

In the early stages of a collision, energy densities exceeding the confinement scale T_C , above which quarks and gluons are not confined into hadrons anymore, are reached. A new, interesting state of matter is formed, the quark-gluon plasma (QGP). Contrary to expectations this plasma behaves like a strongly coupled fluid instead of a weakly coupled gas. This is concluded from the fact that relativistic hydrodynamic calculations work surprisingly well as a description for the dynam-

a) Gold ions at RHIC



b) Lead ions at LHC

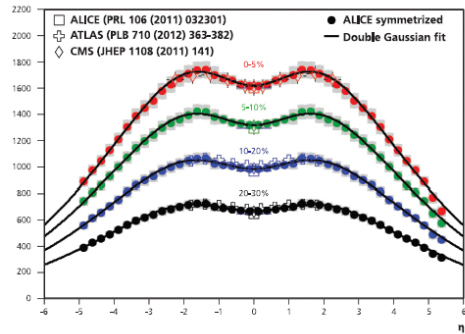


Figure 2: Charged particle multiplicities measured in central HICs by the detectors STAR (at RHIC [3]) and ALICE (at LHC [4])

ical behavior of the plasma. As hydrodynamical calculations give an accurate description already at very early stages, this also suggests that the plasma thermalizes locally very fast, about $t_{therm} \approx \mathcal{O}(1) \frac{\text{fm}}{c}$, which corresponds to 3×10^{-24} seconds after the collision.

This leads to the question, what mechanisms are responsible for this fast thermalization process. In order to find an answer we need to study the early non-equilibrium dynamics of the system. Due to strong coupling calculations cannot be performed in perturbative QCD. This is in principle not a problem for lattice QCD, but this framework is not suited well to treat the dynamics of the collision. Therefore alternative methods are needed. A promising candidate is the AdS/CFT correspondence, described in the next section.

2.2 AdS/CFT correspondence

In modern physics, the gauge/gravity duality provides a link between quantum field theory and quantum gravity. Nearly 20 years ago Maldacena [5] conjectured the equivalence of type IIB superstring theory on $AdS_5 \times S^5$ and $SU(N_c)$ $\mathcal{N}=4$ supersymmetric Yang-Mills theory, a conformal field theory (CFT) on the four dimensional boundary of Anti-de Sitter space (AdS_5). This AdS/CFT correspondence is a realization of the holographic principle introduced by 't Hooft [6] and Susskind [7], which states that for theories with gravity all information within a volume is encoded in a theory without gravity on its boundary. Considering a black hole, calculations show that its entropy (which describes the information

content) is proportional to the area of its event horizon and not its volume. This is expressed in the Bekenstein-Hawking law

$$S_{BH} = \frac{A}{4G_N}, \quad (2.1)$$

where A is the area of the horizon surface and G_N is Newton's constant.

A feature of AdS space is that its boundary is conformal equivalent to Minkowski space. This is the natural geometry to study quantum field theory without gravity. Therefore one can consider the QFT to “live” on the boundary of the AdS space-time in analogy to a hologram, which encodes the image of a three dimensional object in a two dimensional surface. The CFT contains all information of gravity in AdS space of one dimension higher. This connection allows to translate expectation values of operators of the field theory into fields of the gravitational theory and vice versa. Therefore it is possible to perform calculations on either side of the duality and then translate the result to the other side. Because gauge/gravity duality is a weak/strong duality, strongly coupled fields on the field theory side are related to weakly coupled fields on the gravity side and vice versa. This makes many calculations that are very hard (or even impossible due to computational limits) on one side very simple on the other side.

For our purposes, the correspondence is especially useful in the limits of large gauge group rank and large 't Hooft coupling λ . In this particular limit, the full string theory action can be approximated with classical supergravity, which makes calculations much easier. As lattice calculations show (Fig. 3), in the deconfined phase of QCD the thermodynamical quantities only depend slightly on N_c .

In the field of quantum gravity this characteristic of the duality allows to address problems, which were out of reach of perturbation theory. Performing field theory calculations and translating the results to the gravity side gives further insight into quantum gravity and problems, such as the black hole information paradox can be addressed [8]. Another field of research is condensed matter physics, where some phenomena of strongly correlated systems are investigated using generalizations of the AdS/CFT correspondence [9]. Our interest focuses on the applications in quantum field theory, where AdS/CFT can be used to describe strongly coupled dynamical systems, which are currently out of reach for other methods. For example the QGP mentioned before in section 2.1.

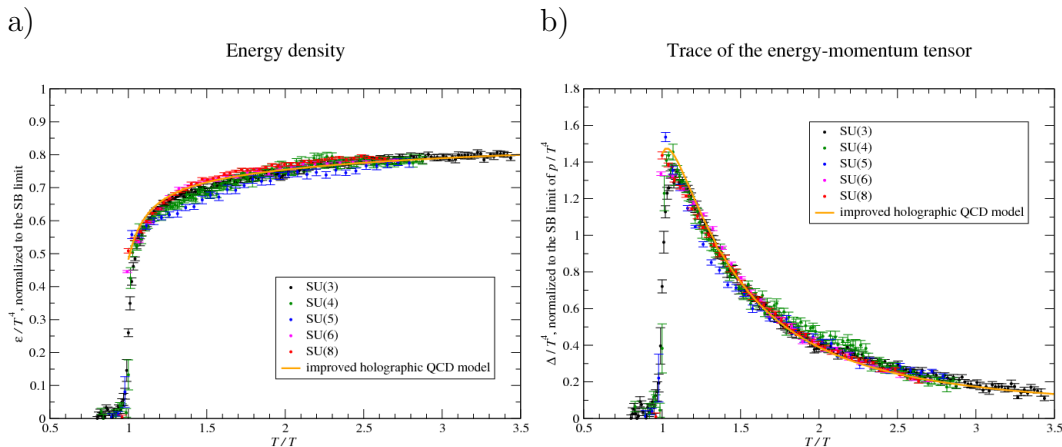


Figure 3: Lattice calculations for the energy and trace anomaly of the QCD plasma at different N_C . [10]

2.3 Holographic description of heavy ion collisions

A conformal field theory, namely $\mathcal{N}=4$ supersymmetric Yang-Mills (SYM) theory, can be seen as a toy model for the deconfined phase of QCD. Fig. 4 shows the phase diagram of QCD. Although $\mathcal{N}=4$ SYM and QCD are rather different theories, at the energies reached in HICs they share some properties. In case of non-zero temperature some differences vanish, which may suggest that SYM is a reasonable toy model for QCD. For instance, above the critical temperature (T_c) QCD is not confined anymore, while $\mathcal{N}=4$ SYM is not confined at all. Further the scales of chiral symmetry breaking and the running coupling constant are not relevant above T_c (as long as T is not asymptotically large), whereas $\mathcal{N}=4$ SYM is a scale invariant theory at any temperature. Also, supersymmetry in $\mathcal{N}=4$ SYM is broken at non-zero temperature. Figure 3a) shows that QCD enters a conformal window above $1.5 T/T_c$, where the energy density increases very slowly. This supports the assumption of strong coupling, as the Stefan-Boltzmann value for the free theory is reached just at asymptotically large temperatures. Further, figure 3b) shows the trace anomaly of the QCD plasma, which decreases for large energies. The trace anomaly is zero in a conformally invariant theory. In HICs the energies are in a region above T_c , where the QGP can be assumed to be conformally invariant.

Additionally, the large N_c limit and the correspondence to AdS_5 make it possible to calculate the ratio of shear viscosity over entropy density $\frac{\eta}{s} = \frac{1}{4\pi}$ [11, 12]. Measurements at the RHIC experiments suggest an upper bound for this ratio of $\frac{\eta}{s} \leq 0.25$ [13]. This holographic result is in much better agreement with this bound than results from perturbative QCD calculations.

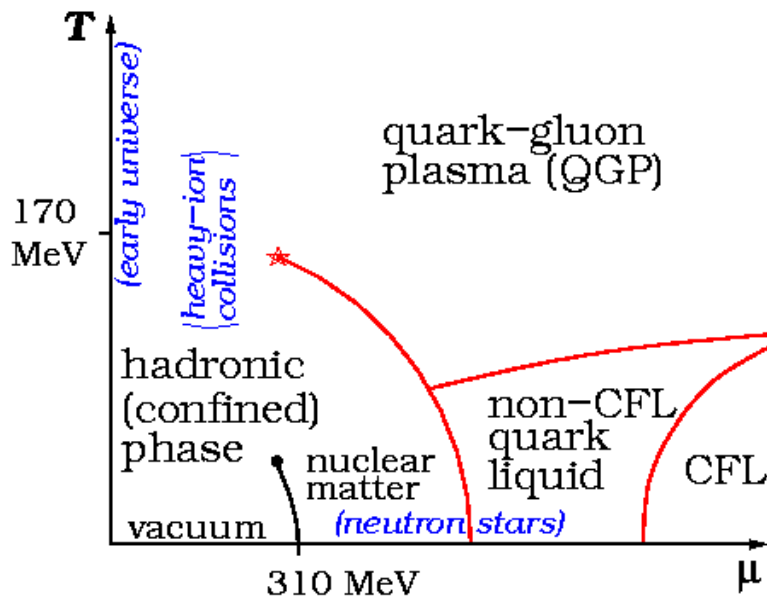


Figure 4: QCD phase diagram with the temperature and chemical potential as axes. Above the critical temperature the deconfined phase (QGP) is reached. [14]

Our purpose is to describe collisions of heavy ions on the gauge theory side. This can be modeled by the collision of gravitational shock waves on the gravity side [15, 16] (for numerical calculations see [17, 18]). Further the formation and thermalization of the plasma corresponds to the formation and equilibration of a black hole. The holographic dictionary allows to extract the expectation value of the energy momentum tensor (EMT) $T_{\mu\nu}$ from these models. This quantity has been extensively studied in a fully dynamical simulation of HICs and gave surprisingly accurate predictions for particle spectra [19].

Going beyond these local observables, we want to study the early time dynamics in such collisions. Therefore we are interested in non-local quantities like two-point functions and the entanglement entropy (EE), introduced in the following section.

2.4 Entanglement entropy

Consider a quantum mechanical or a quantum field theory (QFT) system at zero temperature, which is described by the pure ground state $|\Psi\rangle$. For a non-

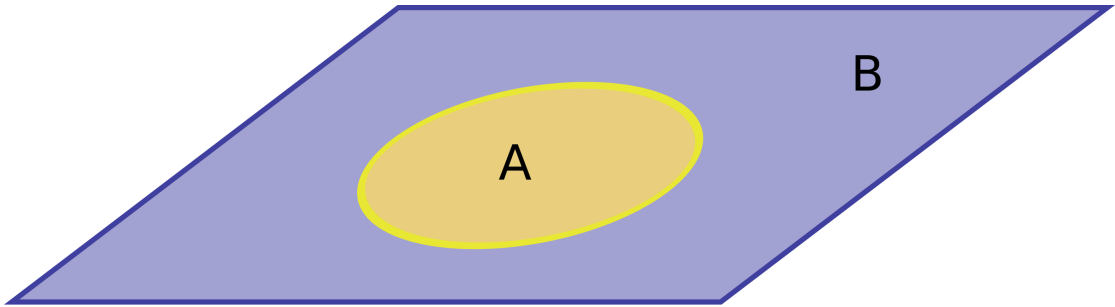


Figure 5: Dividing the system into subsystems A and B .

degenerate wave function $|\Psi\rangle$ the density matrix is given by

$$\rho_{tot} = |\Psi\rangle\langle\Psi|, \quad (2.2)$$

and the von Neumann entropy is zero

$$S_{tot} = -\text{tr}(\rho_{tot} \log \rho_{tot}) = 0. \quad (2.3)$$

If we divide this system into two subsystems A and B (see Fig. 5), we can write the total Hilbert space as direct product of the two Hilbert spaces of the subsystems A and B as follows

$$\mathcal{H}_{tot} = \mathcal{H}_A \otimes \mathcal{H}_B. \quad (2.4)$$

An observer in subsystem A without access to B computes observables with the reduced density matrix ρ_A

$$\rho_A = \text{tr}_B(\rho_{tot}), \quad (2.5)$$

where the trace is taken over the subspace \mathcal{H}_B only. The EE of the subsystem A is defined as the von Neumann entropy of the reduced density matrix ρ_A

$$S_A = -\text{tr}_A(\rho_A \log \rho_A). \quad (2.6)$$

This quantity provides a measure for how strongly entangled the state $|\Psi\rangle$ is. If $|\Psi\rangle$ can be written as a product of two elements of the subspaces, there is no entanglement at all, i.e. $S_A = 0$.

The EE contributes to the understanding of quantum physical phenomena in many fields of physics. For example, in condensed matter physics quantum phase transitions cannot be described with classical quantities, as they do not take entanglement into account. Here EE is a candidate for an order parameter, distinguishing

different phases. Such systems at quantum critical points can be described with conformal field theories. This property justifies the AdS/CFT approach used later on. In two dimensional CFT the EE can be calculated analytically [20, 21]

$$S_A = \frac{c}{3} \log\left(\frac{\xi}{a}\right), \quad (2.7)$$

where ξ is the length of the entangling region, a is a ultraviolet (UV) cutoff and c is the central charge of the CFT.

In this work we want to calculate the EE in HICs in four dimensional $\mathcal{N}=4$ SYM theory, described above in section 2.3. This provides a further quantity to study the dynamics of the system (i.e. SYM plasma), besides the EMT and the two-point function. EE can be used to distinguish different regimes in its evolution.

Calculating the EE in interacting field theories with field theoretical methods is a very hard task, especially in dimensions greater than two. Using the methods of AdS/CFT correspondence, an area law to calculate the EE in d -dimensional static backgrounds was proposed by Ryu and Takayanagi [22]

$$S_A = \frac{\text{Area of } \gamma_A}{4 G_N^{(d+1)}}, \quad (2.8)$$

where $G_N^{(d+1)}$ is Newton's constant in $(d+1)$ dimensions and γ_A denotes the minimal surface in AdS spacetime, which shares its boundary with the subsystem A of the field theory located on the AdS boundary (Fig. 6). This formula was generalized by Hubeny et al. [23] to time dependent backgrounds by generalizing the minimal surface to an extremal one. Looking at the two dimensional result, one can see that the results match and the central charge of the CFT is related to the AdS spacetime via

$$c = \frac{3R}{2G_N^{(3)}}, \quad (2.9)$$

where R is the AdS radius. Comparison of the results in higher dimensions, obtained from free (instead of strongly coupled) CFT, also suggests that the holographic area formula (2.8) can be used.

Further the area law (2.8) looks very similar to the Bekenstein-Hawking entropy of a black hole, if the horizon is considered the dividing boundary of the two subsystems. This suggests that EE may be a candidate for the source of black hole entropy [24, 25].

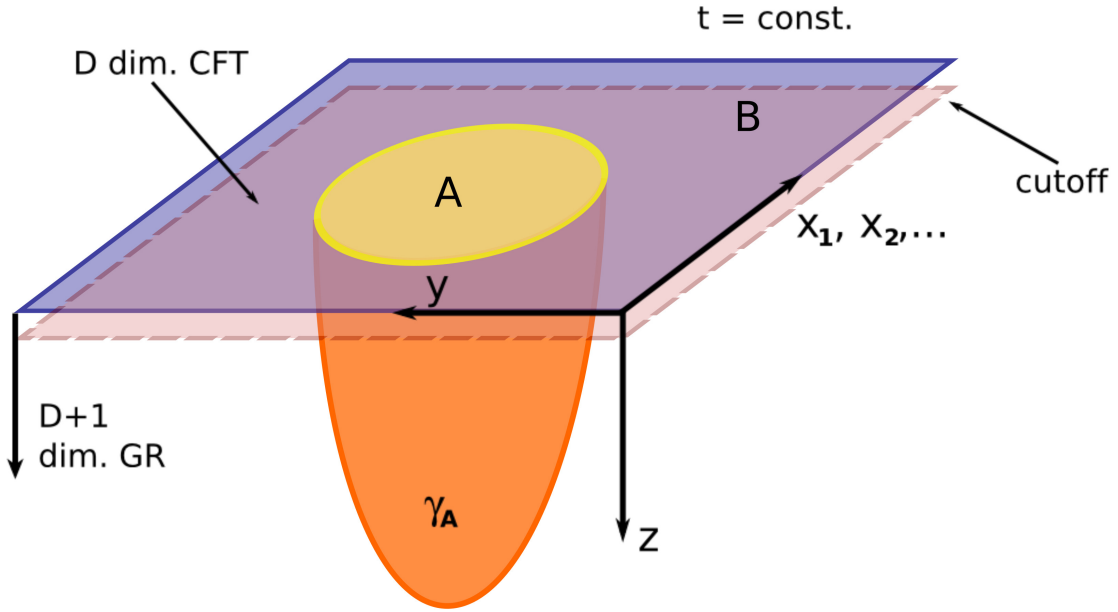


Figure 6: The extremal surface for the EE calculation via the holographic area law.

2.5 Einstein's equations

As we want to perform our calculations on the gravity side of the AdS/CFT correspondence, we need to solve the corresponding Einstein equations. In their most general form they read

$$G_{\mu\nu} + \Lambda g_{\mu\nu} = 8\pi T_{\mu\nu}, \quad (2.10)$$

with the EMT $T_{\mu\nu}$ of the matter fields and the Einstein tensor $G_{\mu\nu}$ describing the geometry, defined with a cosmological constant Λ as

$$G_{\mu\nu} = R_{\mu\nu} - \frac{1}{2} g_{\mu\nu} R, \quad (2.11)$$

where $R_{\mu\nu}$ and R are the Ricci tensor and Ricci scalar respectively and $g_{\mu\nu}$ is the spacetime metric.

In this work, we concentrate on spacetimes which are asymptotically AdS. In d -dimensions AdS space is a maximally symmetric and exact solution to Einstein's equations in vacuum with negative cosmological constant and has constant curvature. In the so called Poincaré patch, the line element is given by

$$ds^2 = \frac{L^2}{r^2} dr^2 + \frac{r^2}{L^2} \eta_{\mu\nu} dx^\mu dx^\nu, \quad (2.12)$$

with $\eta_{\mu\nu}$ being the $(d - 1)$ -dimensional Minkowski metric. For AdS_d the Ricci scalar and the cosmological constant are given by

$$R = \frac{-d(d-1)}{L^2}, \quad (2.13)$$

$$\Lambda = \frac{-(d-1)(d-2)}{2L^2}. \quad (2.14)$$

In the following we work in five dimensions $d = 5$ and set the AdS radius to $L = 1$. In vacuum ($T_{\mu\nu} = 0$) Einstein's equations read

$$R_{MN} - \frac{1}{2}g_{MN}R + \Lambda g_{MN} = 0, \quad (2.15)$$

$$R_{MN} + 4g_{MN} = 0, \quad (2.16)$$

which we will use for our calculations.

3 Solving Einstein's equations numerically

Solving Einstein's equations in general leads to a set of coupled non-linear partial differential equations, which is a highly involved task. In the rare examples where analytic solutions are available, simplifying assumptions such as spatial homogeneity and/or isotropy are imposed. Investigating systems with less (or no) symmetries, usually requires the help of numerical methods. Particularly systems without time-translation invariance, which are relevant for this work, need to be solved numerically.

Since the start in the 1960s [26] numerical relativity made a huge progress. In the 1970s the first simulations of colliding black holes were successfully performed [27]. Since then the development of computers and the improvement of algorithms allowed to tackle more involved problems. Nowadays it is possible to simulate (full) four dimensional systems of binary black holes with strong and dynamical gravitational fields [28]. Of special interest in this field is the calculation of templates for gravitational wave forms which are important to large detection experiments such as LIGO or VIRGO amongst others. The first direct measurements of gravitational waves [29] show very good agreement with the results of numerical simulations.

In contrast to astrophysical applications where Einstein's equations need to be solved on four dimensional Minkowski background, in a holographic setup the equations must be solved on five dimensional AdS spacetime. Although in principle the same numerical techniques may be applicable, for this case there exists a preferable formulation as described in the next section.

3.1 Approaches

Considering dynamical spacetimes, the problem can be divided into the search of initial conditions on a hypersurface and the evolution to neighboring hypersurfaces. Even finding initial conditions can be a complicated task, as they must satisfy constraint equations which are part of Einstein's equations. This can be implemented as an iterative procedure.

The most common approach is called ADM formalism, introduced by Arnowitt, Deser and Misner in the late 1950s [30]. They used a '3+1 decomposition' where spacetime is split into spacelike hypersurfaces and the evolution is performed in the time direction. This corresponds to a Hamiltonian formulation of general relativity.

A different approach is the 'characteristic formulation' where lightlike slices are used for the foliation of spacetime, instead of spacelike slices. Opposed to '3+1 formalisms' which are restricted to a bounded domain, the characteristic formulation was tailored to study radiation at null infinity. This approach turns out to be more convenient in AdS/CFT calculations, since effects at the boundary play an important role.

The biggest advantage of the characteristic formulation is, that Einstein's equations form a nested set of ordinary differential equation (ODE) on the characteristics. The computational implementation of an evolution scheme depends on the version of the formalism and the initial value problem, but most of them have additional advantages in common [31]. For example there are no constraints on the initial conditions and therefore no iterative constraint solvers are needed. Further the characteristics extend to null infinity, so the behavior at the boundary can be described without extrapolations.

3.2 Homogenous isotropization

To demonstrate the procedure of solving Einstein's equations in the characteristic formulation, we first choose a simple setup, a homogeneous but initially anisotropic AdS₅-black hole spacetime [32–35]. On the field theory side this corresponds to a homogeneous but initially anisotropic $\mathcal{N} = 4$ SYM plasma. The equilibrium temperature of this plasma is given by the Hawking temperature of the final black hole on the gravity side. For solving Einstein's equations in vacuum (2.16) we make an ansatz for the metric in Eddington-Finkelstein coordinates, where the anisotropy is specified via the function B

$$ds^2 = -A dv^2 + 2 dr dv + \Sigma^2 e^{-2B} dy^2 + \Sigma^2 e^B (dx_1^2 + dx_2^2), \quad (3.1)$$

where v is the advanced time, r is the holographic coordinate, y is the longitudinal spatial direction and x_1, x_2 are the transversal spatial directions. The functions A , B and Σ are functions of the holographic coordinate r and advanced time v only. In this setting it is easier to see the main advantage of the characteristic formulation. In the case of shock waves the procedure is the same and Einstein's equations simplify to ODEs as well, but there are more terms.

Defining the derivatives along ingoing and outgoing radial null geodesics (i.e. along the characteristics)

$$h' = \partial_r h, \quad (3.2)$$

$$\dot{h} = \partial_v h + \frac{1}{2} A \partial_r h, \quad (3.3)$$

using the metric ansatz (3.1) and inserting it into (2.16), Einstein's equations in vacuum simplify to a nested set of ODEs

$$0 = \Sigma'' + \frac{1}{2} B'^2 \Sigma, \quad (3.4)$$

$$0 = \Sigma (\dot{\Sigma})' + 2 \Sigma' \dot{\Sigma} - 2 \Sigma^2, \quad (3.5)$$

$$0 = \Sigma (\dot{B})' + \frac{3}{2} (\Sigma' \dot{B} + B' \dot{\Sigma}), \quad (3.6)$$

$$0 = A'' + 3 B' \dot{B} - 12 \frac{\Sigma' \dot{\Sigma}}{\Sigma^2} + 4, \quad (3.7)$$

$$0 = \ddot{\Sigma} + \frac{1}{2} (\dot{B}^2 \Sigma - A' \dot{\Sigma}). \quad (3.8)$$

These equations can be solved using an algorithm outlined in [32, 34, 36]. Given B on the initial v -slice, equation (3.4) allows us to calculate Σ . Knowing Σ , equation (3.5) is used to find $\dot{\Sigma}$. Then (3.6) is used to get \dot{B} and (3.7) yields A . Now \dot{B} and A can be used to calculate $\partial_v B$ via (3.3). With this quantity the initial condition ($B(r, v + \Delta v)$) on the next characteristic can be found, using a time integration method like the Runge-Kutta algorithm. The last equation (3.8) is redundant and can be used to check how well Einstein's equations are fulfilled.

3.2.1 Asymptotic behavior

As we are interested in a spacetime which behaves like AdS space asymptotically (i.e. as $r \rightarrow \infty$), we make an expansion of the metric functions near the boundary ($r = \infty$)

$$A(r, v) = r^2 \left(\sum_{i=0}^4 a_i(v) r^{-i} + \mathcal{O}(r^{-5}) \right), \quad (3.9)$$

$$B(r, v) = \sum_{i=0}^4 b_i(v) r^{-i} + \mathcal{O}(r^{-5}), \quad (3.10)$$

$$\Sigma(r, v) = r \left(\sum_{i=0}^4 \sigma_i(v) r^{-i} + \mathcal{O}(r^{-5}) \right). \quad (3.11)$$

The requirement for the spacetime to be asymptotically AdS with conformally flat boundary fixes the first coefficients to $a_0 = 1$, $\sigma_0 = 1$ and $b_0 = 0$. We choose the boundary metric as follows

$$ds^2|_{\text{boundary}} = r^2 (-dt^2 + dy^2 + dx_1^2 + dx_2^2), \quad (3.12)$$

where t denotes the Minkowski time at the boundary.

Inserting the expansion of the metric functions, Einstein's equations can be solved order by order in r . At zeroth order the equations are trivially satisfied. At first order σ_1 remains undetermined and we choose to use the gauge freedom and set

$$\sigma_1(v) = \xi(v), \quad (3.13)$$

where ξ is some arbitrary but fixed function of v . In order to simplify the expressions the argument v is dropped from now on. Up to fourth order all coefficients can be expressed through ξ , but a_4 and b_4 remain undetermined. If higher orders were kept in the expansion, we would see that the fifth order equation constrains a_4 to be independent of v . This constraint coincides with the conservation of energy and momentum. Therefore the asymptotic expansions are

$$A = r^2 + 2r\xi - 2\partial_v\xi + \xi^2 + \frac{a_4}{r^2} - \frac{2a_4\xi}{r^3} + \mathcal{O}(r^{-4}), \quad (3.14)$$

$$B = \frac{b_4}{r^4} - \frac{4b_4\xi}{r^5} + \frac{\partial_v b_4}{r^5} + \mathcal{O}(r^{-6}), \quad (3.15)$$

$$\Sigma = r + \xi - \frac{b_4^2}{7r^7} + \mathcal{O}(r^{-8}). \quad (3.16)$$

A coordinate change from $r \rightarrow z = \frac{1}{r}$ makes the numerical calculation easier, since it relocates the boundary to the finite value $z = 0$.

3.2.2 Redefinition of the metric functions

As one can see in the expressions (3.14) - (3.16) for the metric functions, there are terms diverging when $z \rightarrow 0$ ($r \rightarrow \infty$). This is problematic in the numerical calculation. To avoid this, we make a redefinition of the functions

$$A = \frac{1}{z^2} + \frac{2\xi}{z} + \xi^2 - 2\partial_v\xi + z^2 A_{reg}, \quad (3.17)$$

$$B = z^4 B_{reg}, \quad (3.18)$$

$$\Sigma = \frac{1}{z} + \xi + z^4 \Sigma_{reg}, \quad (3.19)$$

$$\dot{B} = z^3 \dot{B}_{reg}, \quad (3.20)$$

$$\dot{\Sigma} = \frac{1}{2z^2} + \frac{\xi}{z} + \frac{\xi^2}{2} + z^2 \dot{\Sigma}_{reg}. \quad (3.21)$$

Inserting this into Einstein's equations, they can be solved for the regularized functions A_{reg} , B_{reg} , Σ_{reg} , \dot{B}_{reg} and $\dot{\Sigma}_{reg}$ which do not diverge at the boundary.

3.2.3 Holographic relations

The coefficients a_4 and $b_4(v)$ in the asymptotic expansion determine the expectation value of the EMT in the dual field theory [37]

$$\langle T^{\mu\nu} \rangle = \frac{N_c^2}{2\pi^2} \text{diag} [\mathcal{E}, \mathcal{P}_y, \mathcal{P}_{x_1}, \mathcal{P}_{x_2}], \quad (3.22)$$

with the energy density \mathcal{E} and the longitudinal and transversal pressure densities \mathcal{P}_y and \mathcal{P}_{x_i} respectively. From the relations

$$\mathcal{E} = -\frac{3}{4} a_4, \quad \mathcal{P}_y = -\frac{1}{4} a_4 - 2b_4, \quad \mathcal{P}_{x_1} = \mathcal{P}_{x_2} = -\frac{1}{4} a_4 + b_4, \quad (3.23)$$

we can see that the time independence of a_4 translates into a constant energy density, while the pressure components are time dependent due to b_4 . With our choice of the redefinition of the metric functions, these values can conveniently be extracted from A_{reg} and B_{reg} which we compute

$$b_4(v) = B_{reg}(z = 0, v), \quad a_4 = A_{reg}(z = 0, v). \quad (3.24)$$

The fact that the EMT is traceless, arises from the conformally flat boundary metric (3.12). It is also possible to introduce perturbations by imposing time dependent deformations of the boundary geometry. This leads to a conformal anomaly [38] and results in more complicated relations for the components of the field theory EMT [32].

3.2.4 Numerical results

In our simulation we set $\xi = 0$ for convenience but it can also be used to fix the position of the apparent horizon to a specific value as done in [32]. This can be useful, if we want to make sure that the apparent horizon is contained in a restricted computational domain as we do in the shock wave setup.

Using spectral methods (see e.g. [39]), Einstein's equations can be solved on one characteristic. The radial domain of calculation is chosen to be $z \in [0, 1.6]$. For evolution in time, a Runge-Kutta [40] algorithm is used. With the initial profile

$$B_{ini}(0, z) = \beta z e^{-\frac{(z-z_0)^2}{\omega^2}}, \quad (3.25)$$

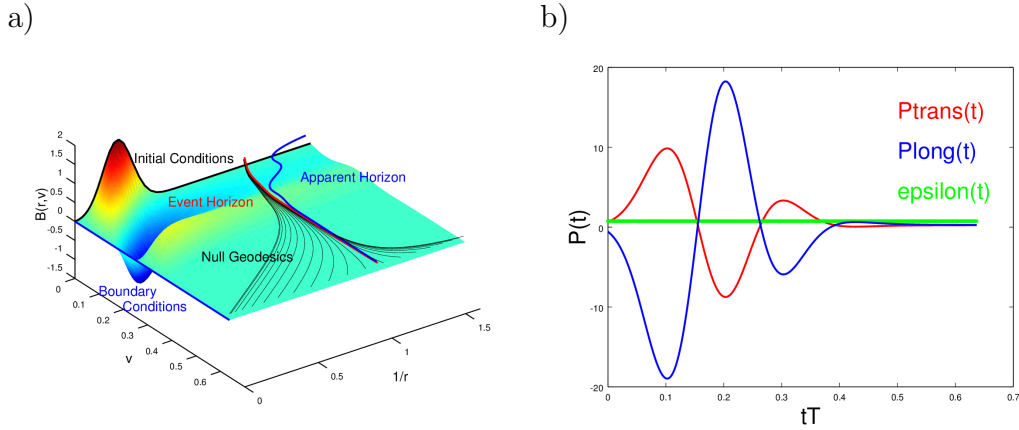


Figure 7: a) Anisotropy function with horizons and geodesics; b) Energy density, transversal and longitudinal pressure.

where $\beta = 6.6$, $z_0 = 0.25$ and $\omega = 0.15$ we find the following results. The Gaussian profile with this shape was chosen, because it suits the purpose to depict the thermalization of the system very well.

The radial location r_H of the apparent horizon is calculated via the condition $\dot{\Sigma}|_{r_H} = 0$ [34]. Opposed to the global concept of an event horizon, the apparent horizon can be determined locally [41, 42]. We take the congruence of null geodesics

$$\frac{dr_G}{dv} = \frac{1}{2} A(r, v), \quad (3.26)$$

and pick the one geodesic which is neither falling into the bulk nor going towards the boundary as an estimate for the event horizon.

In Fig. 7 a) one can see the isotropization of the the system via the function B and the apparent horizon as well as the event horizon and a null congruence of geodesics. Further one can use the relations (3.23) to calculate the components of the EMT on the CFT side. Energy density, longitudinal and transversal pressure are shown in Fig. 7 b). The energy density is constant, whereas the pressure thermalizes after a few oscillations.

The numerical codes are available at www.christianecker.com.

3.3 Shock wave setup

Now that the procedure has been explained in the example above, we can turn our attention to a geometry allowing to describe shock waves. It is worth to mention, that we still use Einstein's equations in vacuum (2.16) (i.e. there are no matter fields involved), as we are dealing with gravitational waves. The metric ansatz to solve them is generalized to [34, 35]

$$ds^2 = -A dv^2 + 2 dr dv + 2 F dv dy + \Sigma^2 e^{-2B} dy^2 + \Sigma^2 e^B dx_1^2 + \Sigma^2 e^B dx_2^2, \quad (3.27)$$

where r is the radial coordinate and A , B , F and Σ are functions of r , the advanced time v and the spatial coordinate y . Now the spacetime is homogeneous and isotropic in two spatial directions (x_1, x_2) and inhomogeneous in y -direction, in which the shock waves propagate. On the field theory side, this is the direction of the 'beam line'.

Inserting the ansatz into (2.16), Einstein's equations read

$$\Sigma'' = -\frac{1}{2} \Sigma (B')^2, \quad (3.28)$$

$$\Sigma^2 F'' = \Sigma (6\tilde{\Sigma} B' + 4\tilde{\Sigma}' + 3F' \Sigma') + \Sigma^2 (3\tilde{B} B' + 2\tilde{B}') - 4\tilde{\Sigma} \Sigma', \quad (3.29)$$

$$12\Sigma^3 \dot{\Sigma}' = e^{2B} (\Sigma^2 (4\tilde{B} F' - 7\tilde{B}^2 - 4\tilde{B} + 2\tilde{F}' + (F')^2) + 2\Sigma (\tilde{\Sigma} (F' - 8\tilde{B}) - 4\tilde{\Sigma}) + 4\tilde{\Sigma}^2) + 24\Sigma^2 (\Sigma^2 - \dot{\Sigma} \Sigma'), \quad (3.30)$$

$$6\Sigma^4 \dot{B}' = e^{2B} (\Sigma^2 (-\tilde{B} F' + \tilde{B}^2 + \tilde{B} - 2\tilde{F}' - (F')^2) + \Sigma (\tilde{\Sigma} (\tilde{B} + 4F') + 2\tilde{\Sigma}) - 4\tilde{\Sigma}^2) - 9\Sigma^3 (\dot{\Sigma} B' + \dot{B} \Sigma'), \quad (3.31)$$

$$2\Sigma^4 A'' = e^{2B} (\Sigma^2 (7\tilde{B}^2 + 4\tilde{B} - (F')^2) + 8\Sigma (2\tilde{B} \tilde{\Sigma} + \tilde{\Sigma}) - 4\tilde{\Sigma}^2) - 2\Sigma^4 (3\dot{B} B' + 4) + 24\dot{\Sigma} \Sigma^2 \Sigma', \quad (3.32)$$

$$6\Sigma^2 \dot{F}' = 3(\Sigma^2 (-(2B' (\tilde{A} + 2\dot{F}) + 2\tilde{A}' + 6\dot{B} \tilde{B} + 4\tilde{B} + A' F')) + 2\Sigma (\Sigma' (\tilde{A} + 2\dot{F}) - 6\dot{B} \tilde{\Sigma} - 4\tilde{\Sigma} - 3\dot{\Sigma} F') + 8\dot{\Sigma} \tilde{\Sigma}), \quad (3.33)$$

$$6\Sigma^2 \ddot{\Sigma} = e^{2B} (\Sigma (2\tilde{B} (\tilde{A} + 2\dot{F}) + \tilde{A} + 2\tilde{F}') + \tilde{\Sigma} (\tilde{A} + 2\dot{F}')) + 3\Sigma^2 (\dot{\Sigma} A' - \dot{B}^2 \Sigma), \quad (3.34)$$

where prime denotes radial derivatives and dot (tilde) denote modified time (longitudinal) derivatives, defined as

$$h' = \partial_r h, \quad \dot{h} = \partial_v h - \frac{1}{2} A \partial_r h, \quad \tilde{h} = \partial_y h + F \partial_r h. \quad (3.35)$$

The equations get more complicated because of the additional function F in the metric and the additional dependence on the coordinate y , but in principle the

scheme remains the same. As in the homogeneous isotropization example we can solve the equations for constant v and then evolve to the next characteristic.

The near boundary expansion works similar to the homogeneous isotropization

$$A = r^2 + 2\xi r + \xi^2 - 2\partial_v \xi + \frac{a_4}{r^2} + \frac{\partial_v a_4 - 4\xi a_4}{2r^3} + \mathcal{O}(r^{-4}), \quad (3.36)$$

$$B = \frac{b_4}{r^4} + \frac{15\partial_v b_4 + 2\partial_r f_4 - 60\xi b_4}{15r^5} + \mathcal{O}(r^{-6}), \quad (3.37)$$

$$F = \partial_r \xi + \frac{f_4}{r^2} + \frac{4\partial_v f_4 + \partial_r a_4 - 10\xi f_4}{5r^3} + \mathcal{O}(r^{-4}), \quad (3.38)$$

$$\Sigma = r + \xi - \frac{4\partial_r f_4 + 3\partial_r a_4}{60r^4} + \mathcal{O}(r^{-5}), \quad (3.39)$$

where the coefficients a_4 , b_4 and f_4 depend on the coordinates v and y . The redefined metric functions are

$$A = \frac{1}{z^2} + \frac{2\xi}{z} + \xi^2 - 2\partial_v \xi + z^2 A_{reg}, \quad (3.40)$$

$$B = z^4 B_{reg}, \quad (3.41)$$

$$F = \partial_y \xi + z^2 F_{reg}, \quad (3.42)$$

$$\Sigma = \frac{1}{z} + \xi + z^4 \Sigma_{reg}, \quad (3.43)$$

$$\dot{B} = z^3 \dot{B}_{reg}, \quad (3.44)$$

$$\dot{\Sigma} = \frac{1}{2z^2} + \frac{\xi}{z} + \frac{\xi^2}{2} + z^2 \dot{\Sigma}_{reg}, \quad (3.45)$$

where we replaced r by $z = \frac{1}{r}$ once again. Inserting these definitions into the nested set of ODEs (i.e. Einstein's equations), obtained from the new metric, allows to find the regularized functions numerically.

Again, we can use the holographic relations described in [37] and find

$$\langle T^{\mu\nu} \rangle = \frac{N_c^2}{2\pi^2} \begin{pmatrix} \mathcal{E} & \mathcal{S} & 0 & 0 \\ \mathcal{S} & \mathcal{P}_y & 0 & 0 \\ 0 & 0 & \mathcal{P}_{x_1} & 0 \\ 0 & 0 & 0 & \mathcal{P}_{x_2} \end{pmatrix} \quad (3.46)$$

with the components determined through the non-zero expansion coefficients

$$\begin{aligned} \mathcal{E} &= -\frac{3}{4} a_4, & \mathcal{P}_y &= -\frac{1}{4} a_4 - 2b_4, \\ \mathcal{P}_{x_1} = \mathcal{P}_{x_2} &= -\frac{1}{4} a_4 + b_4, & \mathcal{S} &= -f_4. \end{aligned} \quad (3.47)$$

In addition to the energy and pressure densities (\mathcal{E} , \mathcal{P}_y and \mathcal{P}_{x_i}) there are off-diagonal elements in (3.46) representing the energy flow \mathcal{S} .

As the numerics are more involved, we used the gauge freedom $\xi(v, y)$ to fix the apparent horizon to $z_{ah} = 1$ and reduced the range of the holographic coordinate to $z \in [0, 1.08]$ [35]. In this geometry, the condition used to fix the apparent horizon gets more complicated too [34].

As initial conditions we choose a superposition of two shock waves with finite energy density and thickness, moving towards each other. To formulate these, it is convenient to use Fefferman-Graham coordinates $(\tilde{r}, \tilde{t}, \tilde{y}, \tilde{x}_1, \tilde{x}_2)$ as in the holographic renormalization. An analytic solution for a single planar shock moving in $\mp y$ -direction is given by

$$ds^2 = \tilde{r}^2 (-d\tilde{t}^2 + d\tilde{y}^2 + d\tilde{x}_2^1 + d\tilde{x}_2^2) + \frac{1}{\tilde{r}^2} (d\tilde{r}^2 + h(\tilde{t} \pm \tilde{y}) (d\tilde{t} \pm d\tilde{y})^2), \quad (3.48)$$

with $h(\tilde{t} \pm \tilde{y})$ an arbitrary function, for which we choose a Gaussian profile of the following form

$$h(v \pm y) = \mu^3 (2\pi\omega^2)^{-\frac{1}{2}} e^{-\frac{1}{2} \frac{(v \pm y)^2}{\omega^2}}, \quad (3.49)$$

with width ω and amplitude μ^3 . As long as the initial shocks are separated far enough, the superposition sufficiently fulfills Einstein's equations. For the calculation, the initial conditions will be transformed to Eddington-Finkelstein coordinates numerically (see [34]).

Using spectral methods and a Runge-Kutta algorithm, we solve the equations for two different initial conditions, the wide and narrow shocks with the parameters of (3.49) being

$$\text{wide : } \mu_w^3 = \frac{4}{3} \omega_w, \quad \omega_w = 0.5, \quad (3.50)$$

$$\text{narrow : } \mu_n^3 = \frac{4}{3} \omega_n, \quad \omega_n = 0.25. \quad (3.51)$$

The centers of both types of shocks are initially located at $\tilde{y}_0 = \pm 1$ and $\tilde{t}_0 = 0$. A motivation for using two different types of shocks, is to model HICs at different energies and therefore different Lorentz contractions.

Fig. 8 shows the energy density for the two different initial conditions. In the regions outside the propagating shocks the energy density is zero as well as in the region between them before the collision. As the shocks collide at $\mu t \approx 1.4$, the

a) narrow shocks

b) wide shocks

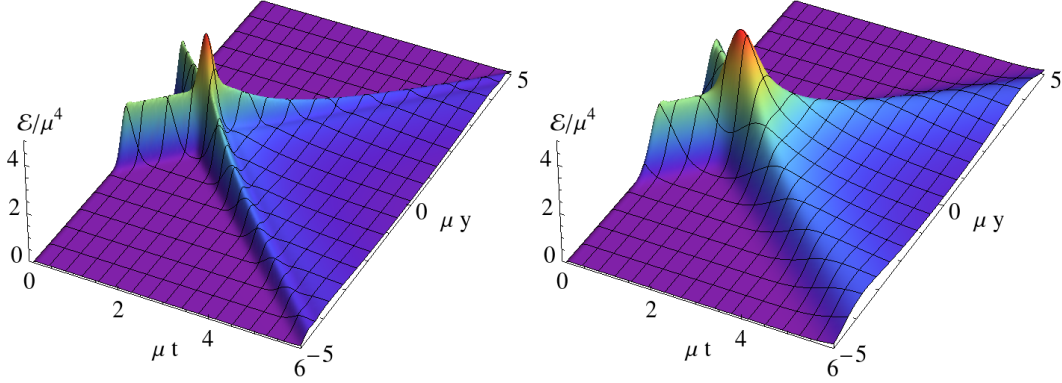


Figure 8: Energy density.

energy density piles up to the central peak in the plot. After the collision, in the forward lightcone, one can see that the energy density is non-zero. The difference between the two cases is the local minimum occurring for narrow shocks. This has been described as 'transparency', because the energy production after the collision is a bit delayed opposed to the 'full stopping' with the hydrodynamic explosion in case of wide shocks [18].

In Fig. 9 we can see how the shape of the apparent horizon evolves in time. To relate this to the shock waves, the energy density is shown as a contour plot below. In the left picture the dip of the horizon is sharper than in the right one, similar to the narrow shocks compared with the wide shocks. In spite of this shape, the horizon in the geometry of wide shocks gets closer to the boundary as the energy density is bigger.

In this setup we can calculate the time evolution of longitudinal and transversal pressure and energy flow as described in (3.47). The results for the transversal pressure are shown in Fig. 10. One can see that there is no transverse pressure before the collision and it is larger for the wide shocks.

Opposed to this Fig. 11 shows that the longitudinal pressure for wide shocks is smaller than for narrow shocks. Further the longitudinal pressure becomes negative right after the collision. This matches the 'transparency' where the outgoing shocks drag the created plasma with them and loosely speaking, it is stretched.

a) narrow shocks

b) wide shocks

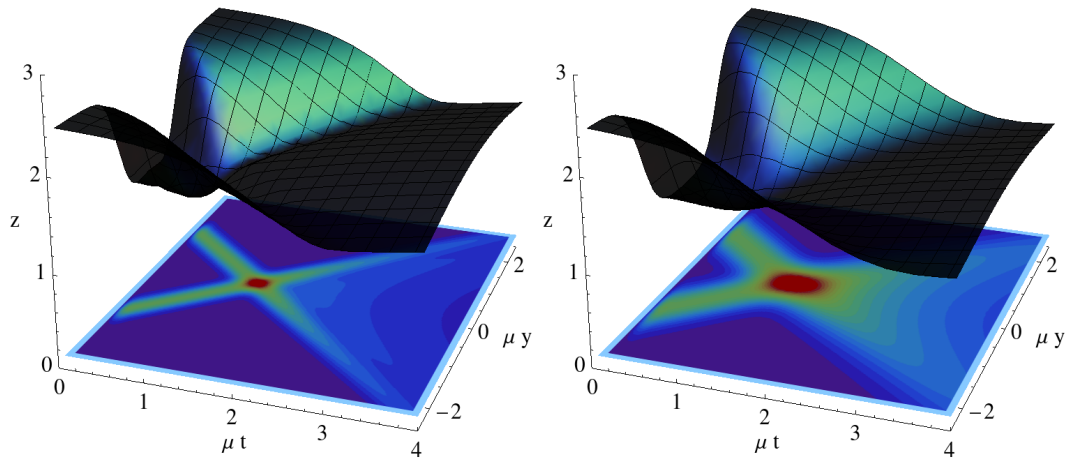


Figure 9: Event horizon over the energy density.

a) narrow shocks

b) wide shocks

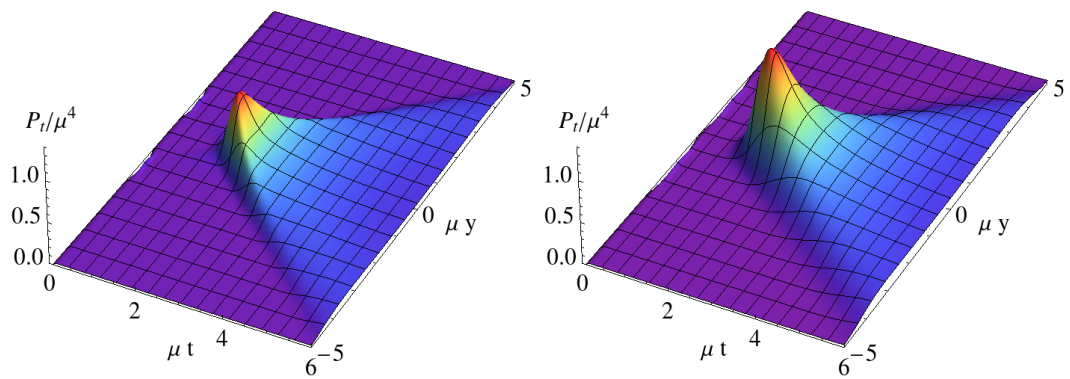


Figure 10: Transversal pressure.

a) narrow shocks

b) wide shocks

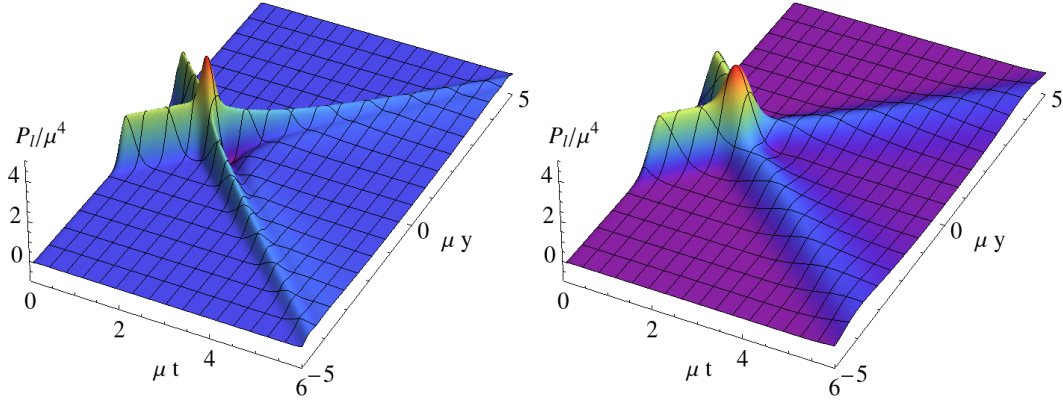
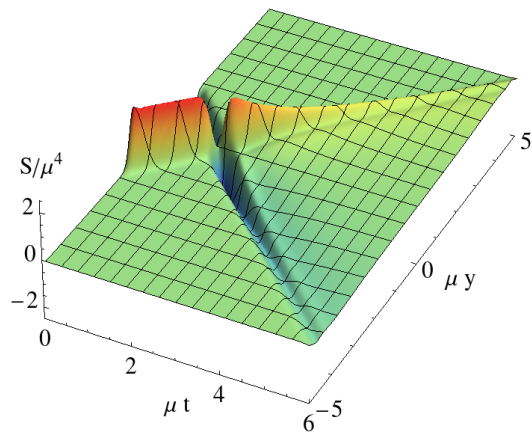


Figure 11: Longitudinal pressure.

Finally Fig. 12 shows the energy flow in the inhomogeneous y -direction. In the other homogeneous directions, there is no energy flow. Similar to the other quantities, the shape is much sharper for the narrow shocks but the values are closer. The negative values are simply energy flowing in the negative y -direction. In this plot one can see that there is no energy flow at the point of the collision, because the amplitudes of the shocks cancel each other. Lastly one can see that the angle of the outgoing energy flow is smaller for the wide shocks, i.e. the particles loose velocity in the collision. This feature appears in all other plots too, but is better visible in the last one.

These calculations were done, using a Mathematica notebook, provided by Wilke van der Schee (<https://sites.google.com/site/wilkevanderschee/>). The numerical values of the functions A , B , F and Σ were used as input for the remainder of this work (i.e. the calculation of two-point functions and the EE).

a) narrow shocks



b) wide shocks

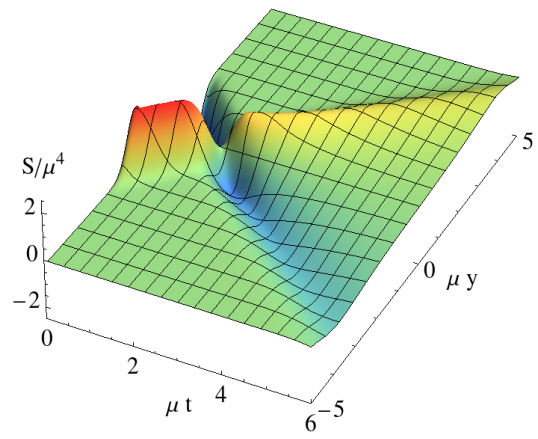


Figure 12: Energy flow.

4 Holographic calculation of two-point functions and entanglement entropy

In the previous chapter, we calculated the EMT of the dual field theory at the boundary of AdS₅. This observable, also called one-point function, is a local quantity that probes the thermalization behavior of the system located at the energy scale set by z . We evaluate $T_{\mu\nu}$ at $z = 0$, which corresponds to the UV regime in the field theory.

To describe the behavior on lower energy scales we need to look at non-local observables, like two-point functions. The calculation of these quantities on the gravity side of the correspondence requires data from different scales z in the bulk. This can give more insight into the dynamics of the system. We compute two-point functions of operators with large conformal weight which correspond to composite operators of many primary fields. Such operators cannot be measured in experiments yet. Nevertheless holography is currently the only framework which allows to compute two-point functions at strong coupling in dimensions higher than two.

To understand the time evolution at the highly anisotropic stages of HICs better we want to calculate another non-local quantity. The EE can be used to study the dynamics of such systems and may turn out to be a measure for thermalization.

It turns out that the calculation of the two-point function and the EE reduces to solving the geodesic equations

$$\ddot{x}^\mu + \Gamma_{\alpha\beta}^\mu \dot{x}^\alpha \dot{x}^\beta = 0, \quad (4.1)$$

where the dot denotes the derivative with respect to an affine parameter. For the actual numerical implementation it is more convenient to use a non-affine parameter σ . With this parametrization (4.1) reads

$$\ddot{x}^\mu + \Gamma_{\alpha\beta}^\mu \dot{x}^\alpha \dot{x}^\beta = -J \dot{x}^\mu, \quad (4.2)$$

where the dot denotes the derivative with respect to σ . For the actual numerical calculation we use an iterative procedure, which needs an ansatz, provided in the following sections.

4.1 The two-point function

The equal time two-point function of an operator \mathcal{O} with large conformal weight Δ is calculated via the path integral [43, 44]

$$\langle \mathcal{O}(t, \vec{x}) \mathcal{O}(t, \vec{x}') \rangle = \int \mathcal{D}\mathcal{P} e^{-i\Delta\mathcal{L}(\mathcal{P})} \approx \sum_{\text{geodesics}} e^{-\Delta L_g} \approx e^{-\Delta L}, \quad (4.3)$$

where the integral is performed over all paths connecting the boundary points (t, \vec{x}) and (t, \vec{x}') through the bulk. The geodesic approximation neglects perturbative corrections and leads to the sum over all geodesics. Due to the large conformal weight, at leading order only the length L of the shortest geodesic contributes, which explains the second approximation. However, the length of all geodesics diverges, as they are attached to the AdS boundary. Therefore we have to regularize the length of the geodesics. We do this by introducing a cutoff in radial direction, such that the geodesics do not end at the infinite boundary but at some finite value close to it

$$\langle \mathcal{O}(t, \vec{x}) \mathcal{O}(t, \vec{x}') \rangle \sim e^{-\Delta L_{reg}}. \quad (4.4)$$

We restrict our attention to geodesics which endpoints are separated in y -direction, although the calculation can be performed in the other directions as well. This amounts to solving the geodesic equation for the subspace with line element

$$ds^2 = -A dv^2 - \frac{2}{z^2} dz dv + 2F dy dv + \Sigma^2 e^{-2B} dy^2. \quad (4.5)$$

To calculate the geodesics, the geometry at every point along the geodesic is needed. As described in the previous chapter, Einstein's equations are solved in a certain coordinate range. This computational domain restricts the number of feasible geodesics to a subset which lies completely in this region.

4.1.1 Geodesic ansatz in pure AdS

The spacetime we are interested in is asymptotically ($z \rightarrow 0$) AdS. Therefore geodesics in pure AdS spacetime provide a good initial guess for the relaxation method described later on. Following [45] we calculate the ansatz, using the line element

$$ds^2 = \frac{1}{z^2} (-dv^2 - 2 dz dv + dy^2). \quad (4.6)$$

Parametrizing the geodesics with the affine parameter τ , we find

$$ds = \frac{1}{z} \sqrt{-\dot{v}^2 - 2\dot{z}\dot{v} + \dot{y}^2} d\tau, \quad (4.7)$$

where the dot denotes the derivative with respect to the affine parameter. Inserting this into the geodesic action

$$S = \int \mathcal{L} d\tau = \int \frac{ds}{d\tau} d\tau = \int \frac{1}{z} \sqrt{-\dot{v}^2 - 2\dot{z}\dot{v} + \dot{y}^2} d\tau \quad (4.8)$$

leads to the geodesic equations of motion, which allow first integrals

$$\frac{\partial \mathcal{L}}{\partial v} - \frac{\partial}{\partial t} \frac{\partial \mathcal{L}}{\partial \dot{v}} = 0 \Rightarrow \frac{-2\dot{v} - 2\dot{z}}{2z\sqrt{-\dot{v}^2 - 2\dot{z}\dot{v} + \dot{y}^2}} = \text{const}, \quad (4.9)$$

$$\frac{\partial \mathcal{L}}{\partial y} - \frac{\partial}{\partial t} \frac{\partial \mathcal{L}}{\partial \dot{y}} = 0 \Rightarrow \frac{2\dot{y}}{2z\sqrt{-\dot{v}^2 - 2\dot{z}\dot{v} + \dot{y}^2}} = \text{const}. \quad (4.10)$$

Using that for spacelike geodesics $g_{\mu\nu} x^\mu x^\nu = 1$ we find

$$\frac{1}{z^2} (-\dot{v}^2 - 2\dot{z}\dot{v} + \dot{y}^2) = 1, \quad (4.11)$$

$$z = \sqrt{-\dot{v}^2 - 2\dot{z}\dot{v} + \dot{y}^2}, \quad (4.12)$$

which simplifies the equations of motion (4.9) and (4.10) to

$$\dot{v} = E z^2 - \dot{z}, \quad (4.13)$$

$$\dot{y} = L z^2, \quad (4.14)$$

$$\dot{z} = \pm z \sqrt{1 - (L^2 - E^2) z^2}, \quad (4.15)$$

where E and L are the constants of motion. To find the geodesic, we use z as parameter and integrate equations (4.13)-(4.15)¹ (for symmetric advanced time we set $E = 0$)

$$z(z) = z, \quad (4.16)$$

$$v(z) = v_0 - z, \quad (4.17)$$

$$y(z) = \pm \sqrt{L^2 - z^2}. \quad (4.18)$$

The second constant of motion L is related to the separation of the geodesic at the boundary via

$$l = (y_+ - y_-)_{z=0} = \frac{2}{L}. \quad (4.19)$$

¹For the equation (4.14) one may write $\dot{y} = \pm \frac{L\dot{z}z}{\sqrt{1-L^2z^2}}$.

For the numerical algorithm it is more convenient to use a non-affine parametrization as follows, which covers both branches of the geodesic at the same time

$$z(\sigma) = \frac{l}{2} (1 - \sigma^2), \quad (4.20)$$

$$y(\sigma) = \frac{l}{2} (\sigma \sqrt{2 - \sigma^2}), \quad (4.21)$$

$$v(\sigma) = v_0 - z(\sigma), \quad (4.22)$$

where $\sigma \in [-1 + \epsilon, 1 - \epsilon]$. We introduced ϵ to realize a UV cutoff at z_{cut} given by

$$\epsilon = 1 - \sqrt{1 - \frac{2 z_{cut}}{l}}. \quad (4.23)$$

To obtain the Jacobian J , needed in the non-affine geodesic equation,

$$J(\sigma) = \frac{d^2\tau}{d\sigma^2} \bigg/ \frac{d\tau}{d\sigma}, \quad (4.24)$$

we integrate equation (4.15)

$$\tau(z) = \int \frac{dz}{z \sqrt{1 - \frac{4}{l^2} z^2}} = \mp \text{artanh} \left(\sqrt{1 - \frac{4}{l^2} z^2} \right), \quad (4.25)$$

and insert the new parametrization to express the affine parameter τ through the non-affine parameter σ

$$\tau(\sigma) = \mp \text{artanh} \left(\sigma \sqrt{2 - \sigma^2} \right). \quad (4.26)$$

Then the Jacobian in (4.2) is given by

$$J(\sigma) = \frac{5\sigma - 3\sigma^3}{2 - 3\sigma^2 + \sigma^4}. \quad (4.27)$$

4.2 The holographic entanglement entropy

The EE [23] for a region A on the AdS-boundary can be calculated via extremizing the surface functional

$$\mathcal{A} = \int d^3\sigma \sqrt{\det \left(\frac{\partial x^\mu}{\partial \sigma^a} \frac{\partial x^\nu}{\partial \sigma^b} g_{\mu\nu} \right)}, \quad (4.28)$$

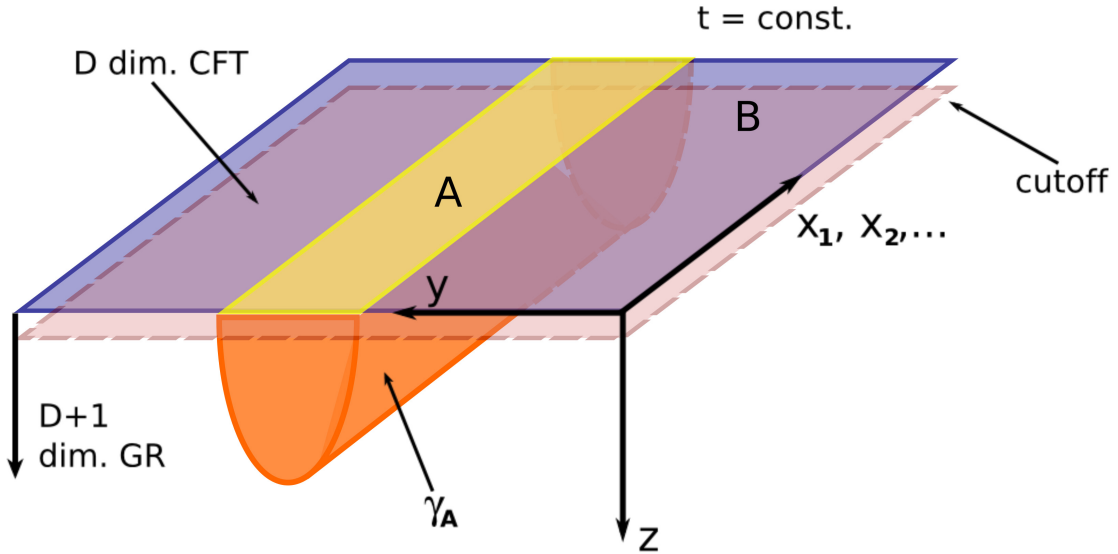


Figure 13: Strip region with minimal surface γ_A .

which has the same boundary as A . The EE in the dual field theory is conjectured to be [22, 23]

$$S_{EE} = \frac{\mathcal{A}}{4G_N}. \quad (4.29)$$

As our spacetime is homogenous only in two spatial dimensions and inhomogeneous in the third one, we restrict our attention to areas, which are stripes with infinite extent in the two x -directions and finite extent in the y -direction (Fig. 13). This simplifies the problem to calculating geodesics in an auxiliary spacetime. The geodesics (and the new ansatz) have to lie inside the calculational domain, as discussed before.

4.2.1 Auxiliary spacetime

We can write the five dimensional line element by introducing auxiliary fields $\phi_i(x^\alpha)$ [45]

$$ds^2 = h_{\alpha\beta} dx^\alpha dx^\beta + \phi_1^2 dx_1^2 + \phi_2^2 dx_2^2, \quad (4.30)$$

where $h_{\alpha\beta}$ is the reduced metric for the coordinates (z, v, y) . Using (4.30) and inserting the parametrization σ the surface functional is given by

$$\mathcal{A} = \int dx_1 \int dx_2 \int d\sigma \sqrt{\phi_1^2 \phi_2^2 h_{\alpha\beta} \frac{\partial x^\alpha}{\partial \sigma} \frac{\partial x^\beta}{\partial \sigma}}. \quad (4.31)$$

As the metric does not depend on the coordinates x_1 and x_2 , we can perform the first two integrals, yielding a constant volume factor. For the considered stripe region, this factor is infinite due to the integral over the infinitely extended transverse directions. Dividing the surface area by that constant factor yields a EE density per Killing volume (i.e. the volume in the homogenous directions).

Due to equation (4.31) our problem is reduced to calculating geodesics in the conformal three dimensional spacetime

$$d\tilde{s}^2 = \tilde{h}_{\alpha\beta} dx^\alpha dx^\beta = \phi_1^2 \phi_2^2 h_{\alpha\beta} dx^\alpha dx^\beta. \quad (4.32)$$

In the present case, the auxiliary fields are given by $\phi_1^2 = \phi_2^2 = \Sigma^2 e^B$, which leads to the auxiliary spacetime

$$d\tilde{s}^2 = \tilde{h}_{\alpha\beta} dx^\alpha dx^\beta = \Sigma^4 e^{2B} (-A dv^2 - \frac{2}{z^2} dz dv + 2 F dy dv + \Sigma^2 e^{-2B} dy^2). \quad (4.33)$$

4.2.2 Geodesic ansatz in the auxiliary spacetime

Similar to the procedure for the two-point function, we look at the metric at asymptotic distances, which looks like

$$ds^2 = \frac{1}{z^6} (-dv^2 - 2 dz dv + dy^2). \quad (4.34)$$

Starting with an affine parametrization, the action is given by

$$S = \int \mathcal{L} d\tau = \int \frac{ds}{d\tau} d\tau = \int \frac{1}{z^3} \sqrt{-\dot{v}^2 - 2 \dot{z} \dot{v} + \dot{y}^2} d\tau, \quad (4.35)$$

and the equations of motion are

$$\frac{\partial \mathcal{L}}{\partial v} - \frac{\partial}{\partial t} \frac{\partial \mathcal{L}}{\partial \dot{v}} = 0 \Rightarrow \frac{-2\dot{v} - 2\dot{z}}{2z^3 \sqrt{-\dot{v}^2 - 2\dot{v}\dot{z} + \dot{y}^2}} = const, \quad (4.36)$$

$$\frac{\partial \mathcal{L}}{\partial y} - \frac{\partial}{\partial t} \frac{\partial \mathcal{L}}{\partial \dot{y}} = 0 \Rightarrow \frac{2\dot{y}}{2z^3 \sqrt{-\dot{v}^2 - 2\dot{v}\dot{z} + \dot{y}^2}} = const. \quad (4.37)$$

With the spacelike condition $g_{\mu\nu} x^\mu x^\nu = 1$ and $E = 0$ we obtain the equations of motion

$$\dot{v} = -\dot{z}, \quad (4.38)$$

$$\dot{y} = L z^6, \quad (4.39)$$

$$\dot{z} = \pm z^3 \sqrt{1 - L^2 z^6}, \quad (4.40)$$

To solve equations (4.38)-(4.40) we use the integral identity

$$\int \frac{dz z^n}{\sqrt{1 - L^2 z^6}} = \frac{z^{1+n}}{1+n} {}_2F_1\left[\frac{1}{2}, \frac{1+n}{6}, 1 + \frac{1+n}{6}; L^2 z^6\right], \quad (4.41)$$

and find the geodesics

$$z(z) = z, \quad (4.42)$$

$$v(z) = v_0 - z, \quad (4.43)$$

$$y(z) = \mp \frac{l}{2} \pm \frac{L z^4}{4} {}_2F_1\left[\frac{1}{2}, \frac{2}{3}, \frac{5}{3}; L^2 z^6\right], \quad (4.44)$$

where $\frac{l}{2}$ is a integration constant, as the hypergeometric function is 0 at the boundary. To guarantee, that the two branches of the geodesic join smoothly, we need to adjust the constant L and express it in terms of the boundary separation l

$$L = \frac{\pi^{\frac{3}{2}} \Gamma[\frac{5}{3}]^3}{8 l^3 \Gamma[\frac{7}{6}]^3}. \quad (4.45)$$

Similar as for the two-point function we choose a non-affine parametrization,

$$z(\sigma) = Z_{max}(1 - \sigma^2), \quad (4.46)$$

$$v(\sigma) = v_0 - z(\sigma), \quad (4.47)$$

$$y(\sigma) = \text{sgn}(\sigma) \left(-\frac{l}{2} + \frac{L z(\sigma)^4}{4} {}_2F_1\left[\frac{1}{2}, \frac{2}{3}, \frac{5}{3}; L^2 z(\sigma)^6\right] \right), \quad (4.48)$$

where the UV-cutoff at z_{cut} is realized by choosing $\sigma \in [-1 + \epsilon, 1 - \epsilon]$ with ϵ

$$\epsilon = 1 - \sqrt{1 - \frac{Z_{UV}}{Z_{max}}}, \quad (4.49)$$

and Z_{max} is the position where the two branches join. Z_{max} is explicitly given by

$$Z_{max} = \frac{2l \Gamma[\frac{7}{6}]^3}{\sqrt{\pi} \Gamma[\frac{5}{3}]^3}. \quad (4.50)$$

To find the Jacobian J we follow the same procedure as above and express τ in terms of σ

$$\tau(z) = \pm \int \frac{dz}{z^3 \sqrt{1 - L^2 z^6}} = \mp \frac{1}{2 z^2} {}_2F_1\left[\frac{1}{2}, -\frac{1}{3}, \frac{2}{3}; L^2 z^6\right], \quad (4.51)$$

$$\tau(\sigma) = \mp \frac{1}{2 Z_{max}^2 (1 - \sigma^2)^2} {}_2F_1\left[\frac{1}{2}, -\frac{1}{3}, \frac{2}{3}; L^2 Z_{max}^6 (1 - \sigma^2)^6\right], \quad (4.52)$$

yielding the Jacobian in (4.2)

$$J(\sigma) = \frac{d^2\tau}{d\sigma^2} \bigg/ \frac{d\tau}{d\sigma} = \frac{-51\sigma + 145\sigma^3 - 205\sigma^5 + 159\sigma^7 - 65\sigma^9 + 11\sigma^{11}}{(2 - \sigma^2)(1 - \sigma^2)(3 - 3\sigma^2 + \sigma^4)(1 - \sigma^2 + \sigma^4)}. \quad (4.53)$$

4.3 Numerical solution of the geodesic equation

The geodesic equations of motion are a set of coupled ordinary differential equations (ODE), which we need to solve in order to find a geodesic. Looking at the boundary conditions, we can specify our problem to be a 'two point boundary value problem', as the endpoints of the geodesic must be attached to the AdS boundary (i.e. at the cutoff). There are two standard methods to solve such a 'two point boundary value problem', shooting and relaxation [40]. Both are iterative procedures. We do not shoot but relax. We choose the relaxation method, because shooting requires careful fine tuning of the initial conditions to hit the second end point, whereas the relaxation method just needs a suitable ansatz. Especially in AdS, where distances grow approaching the boundary, fine tuning is problematic, as small deviations result in chaotic behavior of the result.

In the next section we will describe the relaxation method briefly (for more details see [40]), followed by the concrete application to our set of differential equations in the last part of this chapter.

4.3.1 The relaxation method

The first step is to convert the set of differential equations into finite difference equations (FDE) on a grid, covering our domain of interest. A simple example may look like

$$\frac{dy}{dx} = g(x, y), \quad (4.54)$$

$$\frac{y_k - y_{k-1}}{x_k - x_{k-1}} = g\left(\frac{1}{2}(x_k - x_{k-1}), \frac{1}{2}(y_k - y_{k-1})\right), \quad (4.55)$$

where k denote the grid points. For a system of N first order ODEs converted to FDEs on a grid of size M , a solution consists of values for N functions on M grid points, i.e. of $N \times M$ variables. Using a multidimensional Newton method, the equations are written in matrix form. The matrix has a special block diagonal form, which reduces the resources needed for inverting it to solve the equations.

A set of FDEs may look like

$$0 = E_{j,k} = (y_{j,k} - y_{j,k-1}) - (x_k - x_{k-1}) g_{j,k}\left(\frac{1}{2}(x_k - x_{k-1}), \frac{1}{2}(y_{j,k} - y_{j,k-1})\right), \quad (4.56)$$

where $j = 0, \dots, N-1$ labels the equation and $k = 1, \dots, M-1$ specifies the position x_k . This are N equations at $(M-1)$ points for MN variables. The missing N equations to solve the system are provided by the boundary conditions

$$0 = E_{j,0} = B_j(x_0, y_{j,0}), \quad 0 = E_{j,M} = C_j(x_M, y_{j,M}), \quad (4.57)$$

where B_j contains n_1 boundary conditions at the starting point and C_j provides $n_2 = N - n_1$ boundary conditions at the endpoint (while the remaining entries of B , C and E are zero).

The relaxation method needs an ansatz $y_{j,k}$ for the values of the N variables at the M points. These values are corrected by small increments $\Delta y_{j,k}$, such that $y_{j,k} + \Delta y_{j,k}$ is an improved solution to the FDEs. The new values are then used as ansatz to start all over again until some error criterion is fulfilled. The error may be calculated like

$$err = \frac{1}{NM} \sum_{j,k} \Delta y_{j,k}. \quad (4.58)$$

To find the increments $\Delta y_{j,k}$ we use a multidimensional Taylor expansion of the FDEs to first order

$$\begin{aligned} E_{j,k}(y_{j,k} + \Delta y_{j,k}, y_{j,k-1} + \Delta y_{j,k-1}) &= \\ &= E_{j,k}(y_{j,k}, y_{j,k-1}) + \sum_{n=0}^{N-1} \frac{\partial E_{j,k}}{\partial y_{n,k-1}} \Delta y_{n,k-1} + \sum_{n=0}^{N-1} \frac{\partial E_{j,k}}{\partial y_{n,k}} \Delta y_{n,k}. \end{aligned} \quad (4.59)$$

For a solution, the updated equations $E_{j,k}$ must be zero, therefore we write

$$-E_{j,k} = \sum_{n=0}^{N-1} \hat{S}_{j,n} \Delta y_{n,k-1} + \sum_{n=0}^{N-1} \tilde{S}_{j,n} \Delta y_{n,k}, \quad (4.60)$$

where

$$\hat{S}_{j,n} = \frac{\partial E_{j,k}}{\partial y_{n,k-1}}, \quad \tilde{S}_{j,n} = \frac{\partial E_{j,k}}{\partial y_{n,k}}. \quad (4.61)$$

A similar expansion of the boundary equations leads to

$$-E_{j,0} = \sum_{n=0}^{N-1} \tilde{S}_{j,n} \Delta y_{n,0}, \quad j = n_2, n_2 + 1, \dots, N - 1 \quad (4.62)$$

at the first boundary, where

$$\tilde{S}_{j,n} = \frac{\partial E_{j,0}}{\partial y_{n,0}}. \quad (4.63)$$

At the second boundary we find

$$-E_{j,M} = \sum_{n=0}^{N-1} \hat{S}_{j,n} \Delta y_{n,M-1}, \quad j = 0, \dots, n_2 - 1 \quad (4.64)$$

with

$$\hat{S}_{j,n} = \frac{\partial E_{j,M}}{\partial y_{n,M-1}}. \quad (4.65)$$

Combining $\hat{S}_{j,k}$ and $\tilde{S}_{j,k}$ into one matrix

$$S_{j,n} = \hat{S}_{j,n}, \quad \text{for } n = 0, \dots, N - 1 \quad (4.66)$$

$$S_{j,n} = \tilde{S}_{j,n}, \quad \text{for } n = N, \dots, 2N - 1 \quad (4.67)$$

we get a $N \times 2N$ matrix at every point k . To solve the equations (4.60) above for $\Delta y_{j,k}$ we need to combine all these matrices (like in Fig. 14) and solve the linear equation

$$S.v = b, \quad (4.68)$$

where v is the solution vector related to the corrections $\Delta y_{j,k}$ and b contains the FDEs $E_{j,k}$. The matrix S has now a block diagonal form, which can be dealt with efficiently, using a form of the Gaussian elimination for sparse matrices [40], exploiting the form of S . This makes it possible to tackle problems with large grid sizes and many equations.

In the following section we apply this method to the geodesic equations in the spacetime, obtained in chapter 3.

$$\begin{pmatrix}
X & X & X & . & . & . & . & . & . & . & . & . & . & . & . & . & . \\
X & X & X & . & . & . & . & . & . & . & . & . & . & . & . & . & . \\
I & I & I & X & X & X & . & . & . & . & . & . & . & . & . & . & . \\
I & I & I & X & X & X & . & . & . & . & . & . & . & . & . & . & . \\
I & I & I & X & X & X & . & . & . & . & . & . & . & . & . & . & . \\
. & . & . & I & I & I & X & X & X & . & . & . & . & . & . & . & . \\
. & . & . & I & I & I & X & X & X & . & . & . & . & . & . & . & . \\
. & . & . & I & I & I & X & X & X & . & . & . & . & . & . & . & . \\
. & . & . & . & . & . & I & I & I & X & X & X & . & . & . & . & . \\
. & . & . & . & . & . & I & I & I & X & X & X & . & . & . & . & . \\
. & . & . & . & . & . & I & I & I & X & X & X & . & . & . & . & . \\
. & . & . & . & . & . & . & . & . & I & I & I & X & X & X & . & . \\
. & . & . & . & . & . & . & . & . & I & I & I & X & X & X & . & . \\
. & . & . & . & . & . & . & . & . & . & . & . & I & I & I & X & X & X \\
. & . & . & . & . & . & . & . & . & . & . & . & I & I & I & X & X & X \\
. & . & . & . & . & . & . & . & . & . & . & . & . & . & . & I & I & I
\end{pmatrix}$$

Figure 14: In case of three equations on 6 grid points with two initial conditions at the first grid point and one on the last grid point, the S -matrix looks like this. For better visualization, the I stand for \hat{S} , the X stand for \tilde{S} and the dots represent zeros.

4.3.2 Implementation for the geodesic equation

For applying the relaxation method, it is convenient to use the geodesic equations with non-affine parametrization, as mentioned in sections 4.1 and 4.2

$$\ddot{x}^\mu + \Gamma_{\alpha\beta}^\mu \dot{x}^\alpha \dot{x}^\beta = -J \dot{x}^\mu, \quad (4.69)$$

where J is the Jacobian (equation (4.27) for the two-point function and (4.53) for the EE) and dot denotes the derivative with respect to the non-affine parameter. As these are three second order differential equations (in our reduced spacetime), we need to rewrite them into six first order ODEs. This can be done, introducing the derivatives of the coordinates (z, v, y) as separate variables (p_z, p_v, p_y)

$$p_v = \dot{v}, \quad (4.70)$$

$$\dot{p}_v + \Gamma_{vv}^v p_v^2 + 2\Gamma_{vy}^v p_v p_y + \Gamma_{yy}^v p_y^2 = -J p_v, \quad (4.71)$$

$$p_z = \dot{z}, \quad (4.72)$$

$$\dot{p}_z + \Gamma_{vv}^z p_v^2 + 2\Gamma_{vz}^z p_v p_z + 2\Gamma_{vy}^z p_v p_y + 2\Gamma_{zy}^z p_z p_y + \Gamma_{zz}^z p_z^2 + \Gamma_{yy}^z p_y^2 = -J p_z, \quad (4.73)$$

$$p_y = \dot{y}, \quad (4.74)$$

$$\dot{p}_y + \Gamma_{vv}^y p_v^2 + \Gamma_{vz}^y p_v p_z + 2\Gamma_{vy}^y p_v p_y + 2\Gamma_{zy}^y p_z p_y + \Gamma_{yy}^y p_y^2 = -J p_y. \quad (4.75)$$

To translate this into FDEs, we use a scheme described in (4.55). With the ansatz from sections 4.1 or 4.2, the algorithm can be started (we set the value for the cutoff to $z_{cut} = 0.05$). According to the previous section, we can calculate the matrix S . It turns out that many entries of the blocks are zero. This makes the inversion even more efficient and the corrections are calculated.

An important subtlety is that the correction is only valid for small deviations from the solution (i.e. if the Taylor expansion is valid). To take this into account, we do only apply the full correction if the error (4.58) is small enough (we chose 0.05 for this distinction). Otherwise only 10% of the correction are added to the previous solution.

This whole procedure needs to be repeated until the relative error is sufficiently small (we chose $err < 10^{-6}$ as criterion). If the solution does not converge (e.g. if the initial separation at the boundary and/or the time coordinate are badly conditioned), a computational error will occur eventually. To avoid this, the starting point and the initial separation of the boundary point have to satisfy

$$v_0 \geq \frac{l}{2}, \quad (4.76)$$

in the case of calculating the two-point function. For the EE this condition is modified using the corresponding ansatz. Further the separation l must be small enough, such that the ansatz does not extend the z -range of the calculational domain defined in chapter 3.3.

Once the relaxation was successful, we calculate the length of the geodesic via integration of the line element along the geodesic

$$L_{geo} = \int_{\sigma_{min}}^{\sigma_{max}} d\sigma \sqrt{\dot{x}^\mu(\sigma) \dot{x}^\mu(\sigma) g_{\mu\nu}(x)}, \quad (4.77)$$

using *Mathematicas* functions for interpolation and integration.

The length is directly converted to the two-point function (4.4) or the EE density

$$\frac{S_{EE}}{Vol} = \frac{L}{4G_N}, \quad (4.78)$$

where Vol is the infinite but constant Killing volume of the two remaining spatial coordinates x_1 and x_2 .

5 Results

Using the methods, described in chapter 3, we generate numerical data (i.e. the spacetime metric), prescribing the evolution of spacetime for two different initial conditions, narrow and wide shock waves. These sets of data (i.e. the required Christoffel symbols calculated from it) are used to solve the geodesic equations with the relaxation method described in chapter 4. As already mentioned, we need to solve it in the reduced, three dimensional spacetime to find the two-point function and in the auxiliary spacetime to calculate the EE.

With this setup, it is possible to make different investigations. For example, the width of boundary area of interest can be varied or its spatial position can be changed. As mentioned in chapter 4, we need to take care of the calculational domain. If we choose badly conditioned parameters at the boundary, the geodesics might leave the calculational domain at some point. Solving this problem for all cases treated below involves some trial and error. Especially the early times t are affected as the geodesics bend back in advanced time as well as too large separations l_0 , for which the geometry (further) behind the horizon would be needed. (For the EE the restrictions are stronger than for the two-point function.) For late times the calculations are done up to $t = 5$ as the dynamics caused by the collision has settled in most cases.

For all evolution scenarios, it is useful to take the solution of the previous step as ansatz for the next one, instead of a pure AdS geodesic like initially done.

Boundary coordinates and quantities of the field theory are plotted dimensionless in units of the energy μ while the holographic coordinate is measured in units of the AdS-radius.

5.1 Time evolution of two-point function and entanglement entropy

In this work, we focused on the time evolution of the system first. The whole setup is shown in Fig. 15 and 16 for the two-point function and the EE respectively. The dark surface represents the radial position of the apparent horizon and the energy density of the boundary field theory is displayed as a contour plot located at the cutoff, as already shown in chapter 3.3. In addition, the orange lines show the geodesics calculated, while the green dots depict the initial ansatz. Avoiding the horizon, the tips of geodesics bend towards the boundary and mimic its shape.

a) narrow shocks

b) wide shocks

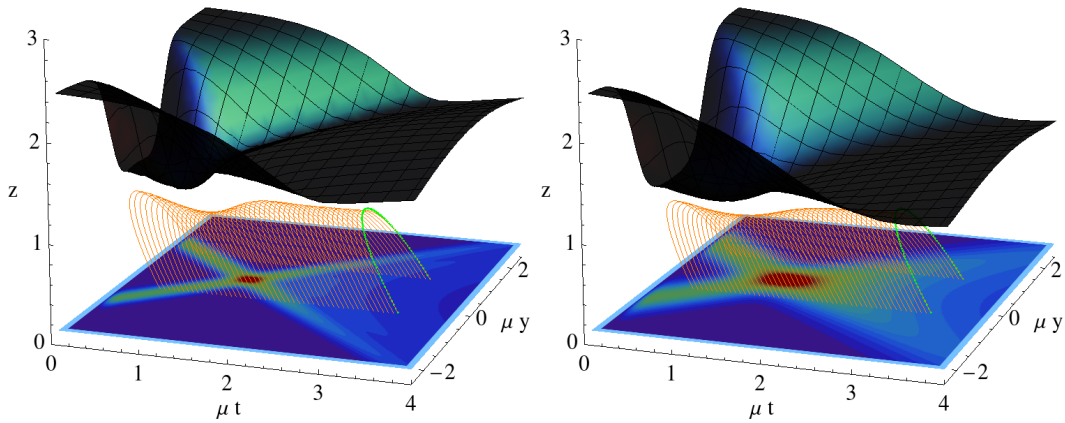


Figure 15: Geodesics (orange curves) and ansatz (green dots) in the three dimensional subspace for calculating the two-point function, the apparent horizon (dark surface) and the energy density (contour plot).

a) narrow shocks

b) wide shocks

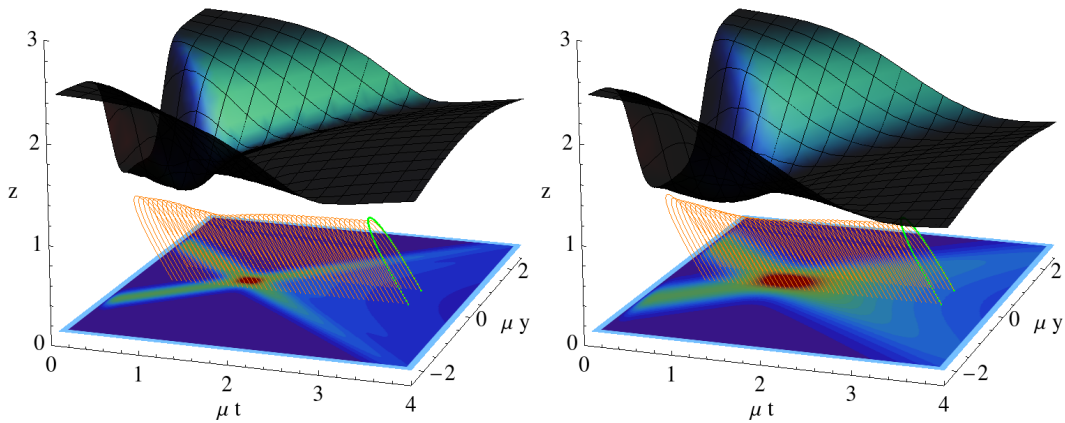


Figure 16: Geodesics (orange curves) and ansatz (green dots) in the auxiliary spacetime for calculating the EE, the apparent horizon (dark surface) and the energy density (contour plot).

A closer look shows that the geodesics calculated in the three dimensional sub-space for the two-point function have a much larger separation at the boundary than the geodesics in the auxiliary spacetime for the EE. In spite of this difference, in both cases the geodesics reach similarly far into the bulk. This makes it obvious why we cannot calculate the EE for as large separations as the two-point functions.

According to chapter 4.3.2, we can calculate the length of the geodesics and therefore conclude the evolution of the two-point function and EE from the evolution of the geodesics. We plot the two-point function (Fig. 17), using equation (4.4) and the entanglement entropy density (Fig. 18), which is directly proportional to the length of the geodesic. The result of this calculation resembles the events of the colliding shock waves.

Looking at the two-point function first (Fig. 17), we can assume that the system is initially in a correlated vacuum state. At least in the case of narrow shocks and sufficiently small separations, the two-point function is 1. For larger separations as well as for wide shocks, the correlations are already destroyed when our time evolution starts. This is due to the restrictions of our possible calculational domain. As the shock waves approach each other, also short range correlations are destroyed. Right before the collision reaches its maximum, most correlations are gone. In the collision, new correlations can form, due to interactions of the shocks and the two-point function grows again. For wide shocks, the correlations grow until the thermal value is approached from below. In the case of narrow shocks, the correlations after the collisions even exceed the correlations before and thermalize to a constant value.

Comparing the time evolution for different separations, we can see a similar behavior for both types of initial conditions. As can be expected on general grounds, the short range correlations are larger than long range correlations. For wide shocks, we see this behavior throughout the whole evolution, while for the narrow shocks things change after the collision. In this case the remaining outward traveling energy density (outgoing shocks) has a stronger influence on long range correlations than on short range ones.

Further, the thermalization occurs earlier, the smaller the separation length was chosen. This mirrors the same behavior described above, namely that short range correlations leave the area of influence of the remaining shocks earlier.

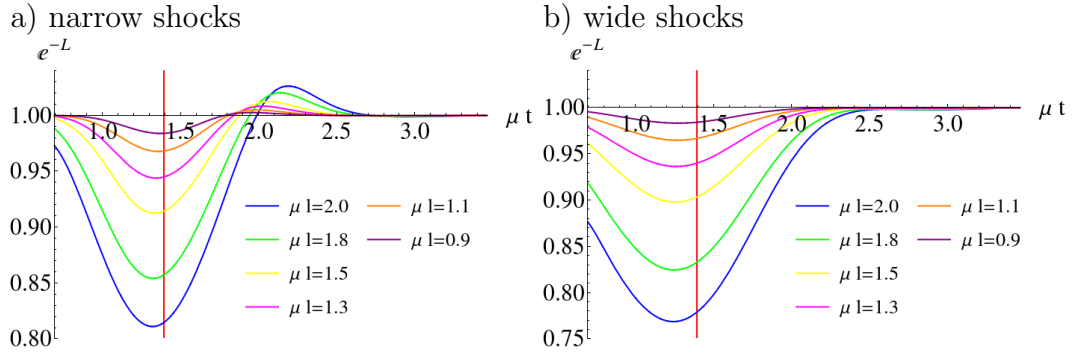


Figure 17: Two-point function for several separations μl . The vertical red line marks the collision time, when the energy density at $y = 0$ reaches its maximum.

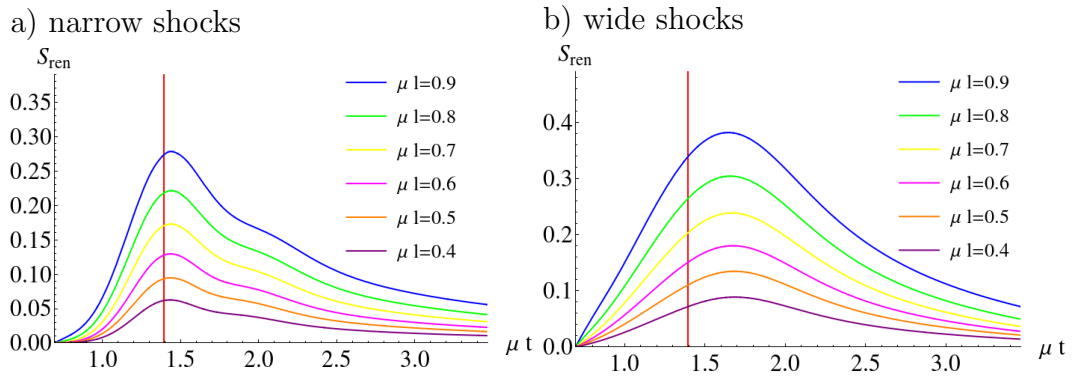


Figure 18: Entanglement entropy for several separations μl . The vertical red line marks the collision time, when the energy density at $y = 0$ reaches its maximum.

To present the results for the EE in the clearest way (Fig. 18) we subtracted the initial value, such that the system starts with zero entanglement. In the time evolution of the EE we can identify four different regions, the *rapid initial growth*, the *linear growth*, the *post collisional regime* and the *late time regime*.

The *rapid initial growth* starts as soon as some energy density enters the entangling region. The growth is faster for the narrow shocks, because the rate at which energy density enters the region is higher. Therefore, the first regime is not very pronounced for the wide shocks, but this might also be owed to the calculational domain, which starts too late.

The *linear growth* follows this initial phase and lasts nearly until the collision reaches its maximum. For larger separations, the slope of this linear growth is steeper.

The maximum EE is reached in the *post collisional regime*, right after the collision. This delay is more pronounced for the wide shocks, where the entanglement falls off without any features. In the case of narrow shocks, a shoulder appears² shortly after the longitudinal pressure has its minimum and the transversal pressure has its maximum (compare 3.3 and Fig. 10a) and 11a)).

The behavior in the *late time regime* can be described by a polynomial fall of

$$S_{EE} \sim t^{-a_{n,w}}, \quad (5.1)$$

where the exponent depends on the initial conditions and the chosen separation l , shown in table 5.1. This late time behavior can be compared to the late time behavior of an effective entropy density

$$s_{eff} = \int_{-\frac{l}{2}}^{-\frac{l}{2}} dy S^3(r_h, t, y), \quad (5.2)$$

where the function S is evaluated at the position of the apparent horizon. The spatial interval of the integration coincides with the entangling region at the boundary. As shown in table 5.1, the coefficient barely depends on the separation. It is expected, that for very late times and large separations, the effective entropy and the EE show the same behavior.

²It turned out that this feature turns into a minimum and an additional maximum, if the initial conditions are changed to even narrower shocks [46].

Table 1: Late time fit for the entanglement entropy.

| | l=0.5 | l=1.0 | l=1.5 |
|-------|-------|-------|-------|
| a_n | 1.84 | 1.82 | 1.80 |
| a_w | 2.07 | 1.95 | 1.78 |

Table 2: Late time fit for the effective entropy.

| | l=0.5 | l=1.0 | l=1.5 |
|-------|-------|-------|-------|
| a_n | 0.94 | 0.95 | 0.96 |
| a_w | 1.14 | 1.14 | 1.14 |

5.2 Tracking a shock wave

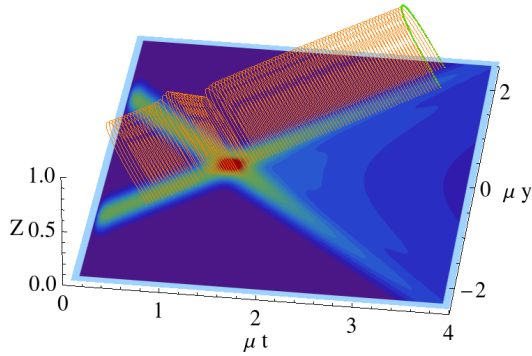
A different approach to observe the time evolution of the system is to follow the center of one shock with the boundary region and calculate the EE. Additionally to the calculation with separation matched to the FWHM of wide and narrow shocks, separations $\mu l = 0.6$ and $\mu l = 0.8$ were used. These separations cover most of the narrow shocks, but only a small part of the wide ones. For the same reason as before, we normalize the EE such that there is no entanglement at the beginning.

The evolution shown in Fig. 19 and 20 has three different parts, as we track the maximum of the energy density of one shock numerically. Looking at the l.h.s. of the figures, we can see that the geodesics follow the incoming shock until the maxima cannot be distinguished anymore. This happens at $\mu t \approx 1.0$ for wide and $\mu t \approx 1.2$ for narrow shocks. In the second part the entangling region stays central until $\mu t \approx 2.1$ ($\mu t \approx 1.6$) when the wide (narrow) shocks separate again. After that it is possible to follow the maximum again. The evolution of the EE is shown on the r.h.s. of the two figures. The transitions between the three parts cause small bumps, as the entangling region changes discontinuously.

Starting with zero entanglement, the EE increases very fast, once the shocks approach each other. For large separations, this growth is even faster than for smaller ones. The evolution in the second part, is identical (except for the normalization) with the results above, because we calculate with a central region again. In the third part, the two different shocks show a qualitatively different behavior, similar to the calculation with central regions described above. For narrow shocks, an additional shoulder³ appears, while the EE of the wide shocks falls off without

³As before, it turned out that this feature turns into a minimum and an additional maximum, if the initial conditions are changed to even narrower shocks [46].

a) geodesics



b) entanglement entropy

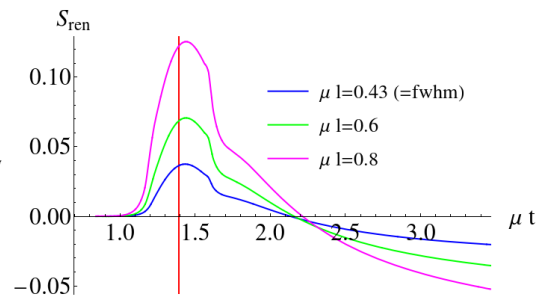
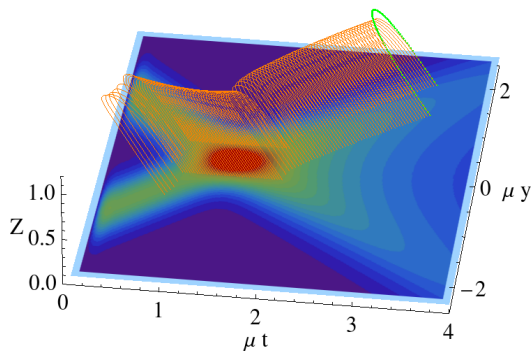


Figure 19: Geodesics (orange) following one of the narrow shocks. The green dots show the initial ansatz and the energy density is shown in the contour plot.

a) geodesics



b) entanglement entropy

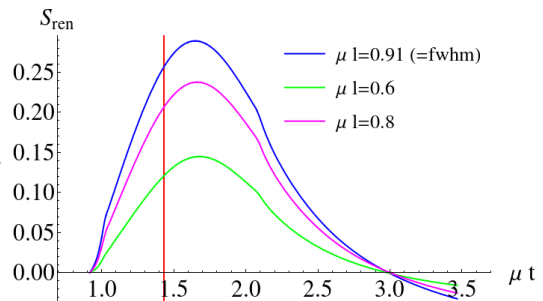


Figure 20: Geodesics (orange) following one of the wide shocks. The green dots show the initial ansatz and the energy density is shown in the contour plot.

any features. The fall off happens in both cases faster than for central regions and even drops below the initial value. This mirrors the behavior of the energy density, which decreases along the moving direction of the shocks, while it increases in the forward light cone of the collision. From a particle perspective, this means that more and more particles leave the light cone and cannot be entangled anymore. The fall off is even faster for larger regions.

5.3 Correlation of two colliding shocks

A last approach of investigating the system is to calculate the correlation between the shocks, instead of two fixed points. Therefore, the endpoints of the geodesics are attached to the centers of the shocks at each point in time. During the collision there are no distinct maxima of the energy density detectable, so the minimal separation was fixed to three times the cutoff. To normalize the two-point function at each time step, we used geodesics in pure AdS with the same separation

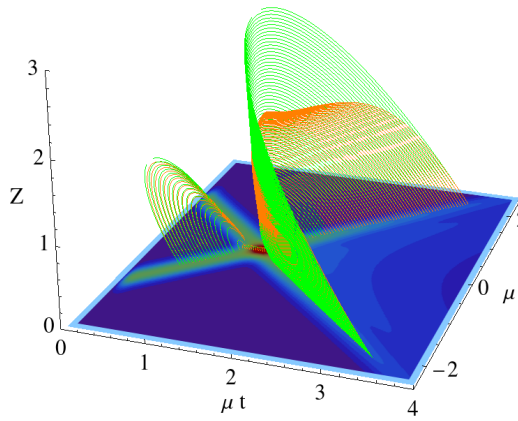
$$\langle \mathcal{O}(t, \vec{x}) \mathcal{O}(t, \vec{x}') \rangle_{normalized} \sim e^{-L+L_0}, \quad (5.3)$$

where L is the length of the geodesic in the shock wave geometry and L_0 is the length of the ansatz in pure AdS spacetime. In Fig. 21 and 22 the setup and the result is shown for narrow and wide shocks respectively.

In both cases the initial growth of the correlation increases linearly until the plateau is reached, although the growth is much faster for the wide shocks. The constant interval accounts to the fixed separation until the shocks separate again. After the collision, the two calculations show a qualitatively different result. While the correlations decrease monotonically for the wide shocks, for narrow shocks they only decrease slightly until a local minimum occurs after the collision and the correlations start to grow again. After some time a maximum is reached and the correlations fall of similar to the wide shocks.

This behavior can be related to the transparency and full stopping scenario discussed in [18]. The correlations increase until the wide shocks are fully stopped and then decrease as a result of the hydrodynamic explosion. For narrow shocks on the other hand, due to the transparency, the shock waves are just altered in shape when passing each other. Shortly after the collision a plasma forms, which causes the further increase of correlations. At some later point in time the shocks are separated so much, that the correlations are destroyed.

a) geodesics



b) two-point function

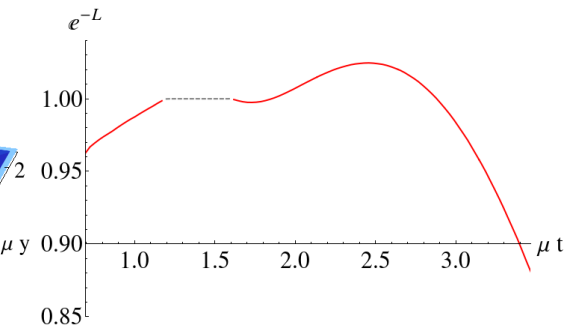
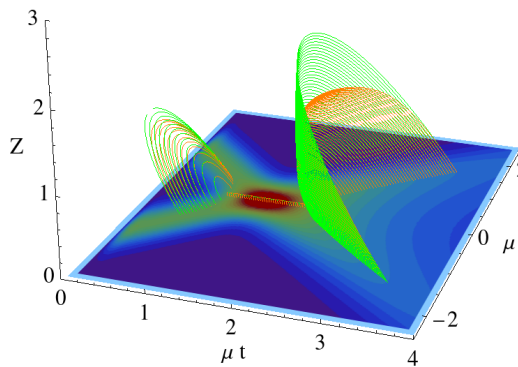


Figure 21: Geodesics (orange curves) attached to the maxima of the narrow shocks (a) for calculating the correlation (b) between them and the energy density (contour plot). The green curves show the pure AdS ansatz which is used for normalization.

a) geodesics



b) two-point function

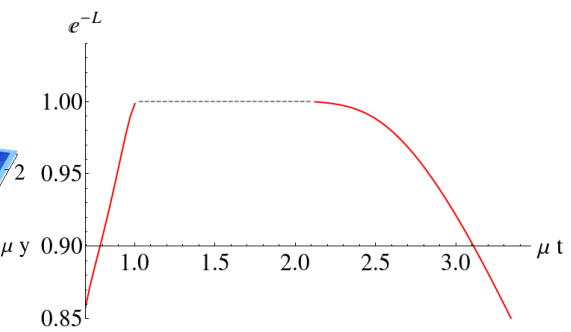


Figure 22: Geodesics (orange curves) attached to the maxima of the wide shocks (a) for calculating the correlation (b) between them and the energy density (contour plot). The green curves show the pure AdS ansatz which is used for normalization.

6 Conclusion and outlook

6.1 Conclusion

In this work we holographically calculated two-point functions of gauge invariant operators with large conformal weight and the EE for colliding gravitational shock waves in AdS_5 . This geometry is mapped holographically to the collision of localized walls of energy in $\mathcal{N}=4$ SYM and can be seen as a toy model for the formation of QGP in HICs.

In our setup, the calculation of the two-point functions and the EE amounts to solving the geodesic equations of motion in particular three-dimensional spacetimes extracted from the AdS_5 shock wave geometry. To do so, we created a Mathematica package, which can be used to investigate the time evolution of these quantities.

We performed the calculations with narrow and wide shocks as initial conditions in order to mimic nuclei at different energies and therefore different Lorentz contractions. It turned out that the system is in a correlated state initially and these correlations between two separated points are destroyed as the shocks approach each other. The minimum is reached right before the shocks overlap completely. New correlations are formed in the collision and the two-point functions grow again. While in the case of wide shocks the correlations are restored and approach the initial value from below, for narrow shocks they exceed this value and settle to the equilibrium value from above.

The EE was normalized to zero at the beginning and grows as the shocks enter the considered entangling region. After the rapid initial growth the EE continues growing in a linear way until a maximum is reached shortly after the collision. After the collision, the EE falls off slowly to the finite value. For the wide shocks this happens without any special features, while in case of narrow shocks there appears an additional shoulder.

Beside the calculations for fixed central separations and entangling regions, we performed calculations for two different approaches. First we took a closer look at the correlations between the shock waves (i.e. the centers of the energy density). As expected, the correlations grow, while the shocks approach each other. After the collision, the correlations fall off for the wide shocks, while they grow again, before falling off for the narrow shocks. For the EE we chose the entangling region in such a way, that it follows one shock.

This scenario mirrors the results obtained before, but also shows, that the EE falls below the initial level after the collision. This can be explained by the fact that the energy density leaves the entangling region faster and the influence of the second shock is further away.

In all calculations we found a qualitatively different behavior for the two initial conditions. Having the transparency and full stopping scenario in mind, this suggests to use the EE as order parameter for the transition between these two regimes.

6.2 Outlook

While writing this work, we got another set of initial conditions, even narrower shocks than described above. Although the results are not included here, all calculations described in this work were also performed for these initial data. The combined results can be found in [46].

A minor extension would be to generate geometries in which the shocks collide at a later time. This would allow to get more insight into the early time behavior, which is excluded due to limitations of the calculational domain. Further, normalizing the energy densities of the shock to those of real HICs would be a small adjustment to this setup.

As we have shown in our work, the interplay between the components of the EMT and the two-point function and the EE is rather complicated and hard to study in the shock wave geometry. It would be interesting to use simpler, homogeneous geometries where the connection between the EMT and the correlations and entanglement in the system should be more obvious. This would allow us to find qualitative relations between the time evolution of the EMT and the two-point function and the EE.

Going beyond the current setup, possible interesting extensions of this work are as follows:

- An obvious drawback of our approach was the assumption of infinite coupling, while in real HICs the coupling is large, but not infinite. Including finite coupling corrections would amount to including string corrections in the corresponding gravity action resulting in modified equations of motion. It would be interesting to study the influence of such corrections on observables like the EMT.

- Another point is that we calculate the two-point function only in the geodesic approximation. A possible extension would be to compute exact two-point functions for operators sourced by an additional scalar field in the bulk. This amounts to performing the gravity calculation with a non-vanishing EMT in the bulk and solving the equations of motion for the scalar field coupled to the metric.
- In our setup we calculate the EE for infinite stripe regions where the computation reduces to finding geodesics in an auxiliary spacetime. For more general regions, e.g. compact regions like a sphere, one has to find genuine extremal surfaces. This is a much harder task than solving the geodesic equations. Existing tools (like surface evolver [47]) for doing this could be used, but need to be adapted for our system. This would allow to investigate the shape dependence of the EE in the shock wave setup along the lines of [48].

A The relaxationPackage

As part of this work we created a Mathematica package for the relaxation of geodesics. The files are accessible at www.christianecker.com. In this appendix we will briefly describe the functionality and how to use it.

The main function of the package is to perform the relaxation method to solve the geodesic equations for a given geometry. As described in chapter 4, the geometry is either given by equation (4.5) for calculating the two-point function or equation (4.33) for the EE. The ansatz for the solution is a geodesic in pure AdS spacetime or in a geometry conformal to AdS, according to chapter 4. In the future, the functionality will be extended to other asymptotically AdS geometries (like the homogeneous isotropization or boost invariant systems).

To study the time evolution, we simply use the calculated geodesic for one point in time as ansatz for the next relaxation, a small time step later. This reduces the amount of iterations opposed to using a new pure AdS ansatz, if the step size is small enough.

How to use the relaxationPackage

To use the package, one first needs the geometry data as input. This data is created by solving Einstein's equations using the Mathematica notebooks of Wilke van der Schee, as described in chapter 3. The data file must contain the metric functions A , B , F and Σ and the gauge function ξ in a certain structure

```
Put[{Aarray, Barray, Farray, Sarray, ksiarray, zarray, yarray},  
    "narrowShocks.ini"];
```

such that they can be interpolated after loading them. The arrays containing the metric functions look like this

```
Aarray = {{z1, t1, y1, A[1, 1, 1]}, {z2, t1, y1, A[2, 1, 1]}, ...}
```

In a new notebook, the package must be loaded and the initialization function with the location of the data file must be called.

Then the parameters for the calculation have to be defined: `gridsize`, `cutoff` z_{cut} , separation of the geodesic (start, end, number of steps), time parameters (start, end, number of steps), error criteria for the iteration to stop (and the shift along the y -direction).

Then the function “relaxOneGeodesic“ will calculate the solution to the geodesic equation at the start time and show the result as well as the apparent horizon in a plot. Further the length of the geodesic is calculated. This function is mainly used to check if the parameters are chosen correctly and to get a first impression of the result.

All of the following functions will return the geodesics in pure AdS spacetime and in the geometry used as input with all relevant parameters. For instance

```
geodesic [[ j ]]= { t , l0 , gridSize , Z , T , Y , errorFDE , iterations , geoLength } .
```

- relaxTevolution
- relaxCorrelation
- relaxFollowShock
- relaxLevolution

The first three functions were used to create the results shown in chapter 5. The last function performs the evolution of a geodesic with increasing separation at the start point t_0 .

The results of the last run are stored in a log file while running, such that they can be accessed if an error occurs during the calculation (mostly because the separation is too large at some point or the domain of calculation is too small).

A downside of using the ”EDCRGTC“-package is that one has to quit the kernel and reload the *relaxationPackage* before loading a new initial data file.

References

- [1] Brookhaven National Laboratory. Relativistic heavy ion collider (rhic) begins smashing atoms, 2000. URL <https://www.bnl.gov/newsroom/news.php?a=11052>. [Online; accessed 17-March-2016].
- [2] Berkeley Lab. Large hadron collider pauses protons; looks ahead to lead, 2010. URL <http://newscenter.lbl.gov/2010/11/04/lhc-lead/>. [Online; accessed 17-March-2016].
- [3] Jorge Casalderrey-Solana, Hong Liu, David Mateos, Krishna Rajagopal, and Urs Achim Wiedemann. Gauge/String Duality, Hot QCD and Heavy Ion Collisions. 2011.
- [4] CERN ALICE Collaboration. More details on the alice v0 detector. URL <http://alipub-dev.web.cern.ch/detectors/more-details-alice-v0-detector>. [Online; accessed 17-March-2016].
- [5] Juan Martin Maldacena. The large N limit of superconformal field theories and supergravity. *Int.J.Theor.Phys.*, 38:1113–1133, 1999. doi: 10.1023/A:1026654312961.
- [6] G. 't Hooft. A planar diagram theory for strong interactions. *Nuclear Physics B*, 72:461–473, April 1974. doi: 10.1016/0550-3213(74)90154-0.
- [7] L. Susskind. The world as a hologram. *Journal of Mathematical Physics*, 36: 6377–6396, November 1995. doi: 10.1063/1.531249.
- [8] S. W. Hawking. Information loss in black holes. *Phys. Rev.*, D72:084013, 2005. doi: 10.1103/PhysRevD.72.084013.
- [9] Sean A. Hartnoll. Lectures on holographic methods for condensed matter physics. *Class. Quant. Grav.*, 26:224002, 2009. doi: 10.1088/0264-9381/26/22/224002.
- [10] Marco Panero. Thermodynamics of the QCD plasma and the large-N limit. *Phys. Rev. Lett.*, 103:232001, 2009. doi: 10.1103/PhysRevLett.103.232001.
- [11] G. Policastro, Dan T. Son, and Andrei O. Starinets. The Shear viscosity of strongly coupled N=4 supersymmetric Yang-Mills plasma. *Phys. Rev. Lett.*, 87:081601, 2001. doi: 10.1103/PhysRevLett.87.081601.
- [12] P. Kovtun, Dan T. Son, and Andrei O. Starinets. Viscosity in strongly interacting quantum field theories from black hole physics. *Phys. Rev. Lett.*, 94: 111601, 2005. doi: 10.1103/PhysRevLett.94.111601.

- [13] M. Ammon and J. Erdmenger. *Gauge/Gravity Duality: Foundations and Applications*. Cambridge University Press, 2015. ISBN 9781107010345. URL <https://books.google.at/books?id=G00soAEACAAJ>.
- [14] Wikipedia. Qcd matter — wikipedia, the free encyclopedia, 2016. URL https://en.wikipedia.org/w/index.php?title=QCD_matter&oldid=707870839. [Online; accessed 17-March-2016].
- [15] Romuald A. Janik and Robert B. Peschanski. Asymptotic perfect fluid dynamics as a consequence of Ads/CFT. *Phys.Rev.*, D73:045013, 2006. doi: 10.1103/PhysRevD.73.045013.
- [16] Daniel Grumiller and Paul Romatschke. On the collision of two shock waves in AdS_5 . *JHEP*, 0808:027, 2008. doi: 10.1088/1126-6708/2008/08/027.
- [17] Paul M. Chesler and Laurence G. Yaffe. Holography and colliding gravitational shock waves in asymptotically AdS_5 spacetime. *Phys.Rev.Lett.*, 106:021601, 2011. doi: 10.1103/PhysRevLett.106.021601.
- [18] Jorge Casalderrey-Solana, Michal P. Heller, David Mateos, and Wilke van der Schee. From full stopping to transparency in a holographic model of heavy ion collisions. *Phys.Rev.Lett.*, 111:181601, 2013. doi: 10.1103/PhysRevLett.111.181601.
- [19] Wilke van der Schee, Paul Romatschke, and Scott Pratt. Fully Dynamical Simulation of Central Nuclear Collisions. *Phys. Rev. Lett.*, 111(22):222302, 2013. doi: 10.1103/PhysRevLett.111.222302.
- [20] Christoph Holzhey, Finn Larsen, and Frank Wilczek. Geometric and renormalized entropy in conformal field theory. *Nucl. Phys.*, B424:443–467, 1994. doi: 10.1016/0550-3213(94)90402-2.
- [21] Pasquale Calabrese and John L. Cardy. Entanglement entropy and quantum field theory. *J.Stat.Mech.*, 0406:P06002, 2004. doi: 10.1088/1742-5468/2004/06/P06002.
- [22] Shinsei Ryu and Tadashi Takayanagi. Holographic derivation of entanglement entropy from ads/cft. *Phys.Rev.Lett.*, 96:181602, 2006. doi: 10.1103/PhysRevLett.96.181602.
- [23] Veronika E. Hubeny, Mukund Rangamani, and Tadashi Takayanagi. A covariant holographic entanglement entropy proposal. *JHEP*, 0707:062, 2007. doi: 10.1088/1126-6708/2007/07/062.

- [24] Luca Bombelli, Rabinder K. Koul, Joochan Lee, and Rafael D. Sorkin. A Quantum Source of Entropy for Black Holes. *Phys. Rev.*, D34:373–383, 1986. doi: 10.1103/PhysRevD.34.373.
- [25] Mark Srednicki. Entropy and area. *Phys. Rev. Lett.*, 71:666–669, 1993. doi: 10.1103/PhysRevLett.71.666.
- [26] Susan G Hahn and Richard W Lindquist. The two-body problem in geometrodynamics. *Annals of Physics*, 29(2):304–331, 1964. doi: 10.1016/0003-4916(64)90223-4.
- [27] Larry Smarr, Andrej Čadež, Bryce DeWitt, and Kenneth Eppley. Collision of two black holes: Theoretical framework. *Physical Review D*, 14(10):2443–2452, 1976. doi: 10.1103/physrevd.14.2443.
- [28] Frans Pretorius. Evolution of binary black hole spacetimes. *Phys. Rev. Lett.*, 95:121101, 2005. doi: 10.1103/PhysRevLett.95.121101.
- [29] B. P. Abbott et al. Observation of Gravitational Waves from a Binary Black Hole Merger. *Phys. Rev. Lett.*, 116(6):061102, 2016. doi: 10.1103/PhysRevLett.116.061102.
- [30] R. Arnowitt, S. Deser, and C. W. Misner. *Gravitation: An Introduction to Current Research*. John Wiley, New York, 1962.
- [31] Jeffrey Winicour. Characteristic evolution and matching. *Living Reviews in Relativity*, 15(2), 2012. doi: 10.1007/lrr-2012-2. URL <http://www.livingreviews.org/lrr-2012-2>.
- [32] Paul M. Chesler and Laurence G. Yaffe. Horizon formation and far-from-equilibrium isotropization in supersymmetric Yang-Mills plasma. *Phys. Rev. Lett.*, 102:211601, 2009. doi: 10.1103/PhysRevLett.102.211601.
- [33] Paul M. Chesler and Laurence G. Yaffe. Boost invariant flow, black hole formation, and far-from-equilibrium dynamics in $N = 4$ supersymmetric Yang-Mills theory. *Phys. Rev.*, D82:026006, 2010. doi: 10.1103/PhysRevD.82.026006.
- [34] Paul M. Chesler and Laurence G. Yaffe. Numerical solution of gravitational dynamics in asymptotically anti-de Sitter spacetimes. *JHEP*, 1407:086, 2014. doi: 10.1007/JHEP07(2014)086.
- [35] Wilke van der Schee. Gravitational collisions and the quark-gluon plasma. 2014.

- [36] Michal P. Heller, David Mateos, Wilke van der Schee, and Miquel Triana. Holographic isotropization linearized. *JHEP*, 1309:026, 2013. doi: 10.1007/JHEP09(2013)026.
- [37] Sebastian de Haro, Sergey N. Solodukhin, and Kostas Skenderis. Holographic reconstruction of space-time and renormalization in the AdS / CFT correspondence. *Commun.Math.Phys.*, 217:595–622, 2001. doi: 10.1007/s002200100381.
- [38] M. Henningson and K. Skenderis. The Holographic Weyl anomaly. *JHEP*, 07:023, 1998. doi: 10.1088/1126-6708/1998/07/023.
- [39] J.P. Boyd. *Chebyshev and Fourier Spectral Methods: Second Revised Edition*. Dover Books on Mathematics. Dover Publications, 2001. ISBN 9780486411835. URL <http://books.google.at/books?id=1EWnQWyzLQYC>.
- [40] William H. Press, Saul A. Teukolsky, William T. Vetterling, and Brian P. Flannery. *Numerical Recipes 3rd Edition: The Art of Scientific Computing*. Cambridge University Press, New York, NY, USA, 3 edition, 2007. ISBN 0521880688, 9780521880688.
- [41] Ivan Booth. Black hole boundaries. *Can. J. Phys.*, 83:1073–1099, 2005. doi: 10.1139/p05-063.
- [42] E. Poisson. *A Relativist’s Toolkit: The Mathematics of Black-Hole Mechanics*. Cambridge University Press, 2007. ISBN 9780521537803. URL http://books.google.at/books?id=5_WaPwAACAAJ.
- [43] Vijay Balasubramanian and Simon F. Ross. Holographic particle detection. *Phys. Rev.*, D61:044007, 2000. doi: 10.1103/PhysRevD.61.044007.
- [44] Guido Festuccia and Hong Liu. Excursions beyond the horizon: Black hole singularities in Yang-Mills theories. I. *JHEP*, 04:044, 2006. doi: 10.1088/1126-6708/2006/04/044.
- [45] Christian Ecker, Daniel Grumiller, and Stefan A. Stricker. Evolution of holographic entanglement entropy in an anisotropic system. *JHEP*, 07:146, 2015. doi: 10.1007/JHEP07(2015)146.
- [46] Christian Ecker, Daniel Grumiller, Stefan A. Stricker, Philipp Stanzer, and Wilke van der Schee. Monitoring shock wave collisions with nonlocal observables. *Manuscript in preparation*, 2016.
- [47] Kenneth A. Brakke. The surface evolver. *Experimental Mathematics*, Vol. 1, no. 2:141–165, 1992. doi: 10.1023/A:1026654312961.

- [48] Piermarco Fonda, Domenico Seminara, and Erik Tonni. On shape dependence of holographic entanglement entropy in $\text{AdS}_4/\text{CFT}_3$. *JHEP*, 12:037, 2015. doi: 10.1007/JHEP12(2015)037.